

*Annual Review of Fluid Mechanics*

# From Bypass Transition to Flow Control and Data-Driven Turbulence Modeling: An Input–Output Viewpoint

Mihailo R. Jovanović

Ming Hsieh Department of Electrical and Computer Engineering, University of Southern California, Los Angeles, California 90089, USA; email: mihailo@usc.edu

Annu. Rev. Fluid Mech. 2021. 53:311–45

First published as a Review in Advance on October 5, 2020

The *Annual Review of Fluid Mechanics* is online at [fluid.annualreviews.org](https://fluid.annualreviews.org)

<https://doi.org/10.1146/annurev-fluid-010719-060244>

Copyright © 2021 by Annual Reviews.  
All rights reserved

## Keywords

input–output analysis, flow modeling and control, physics-aware data-driven modeling, stochastic dynamics, frequency responses, transition to turbulence, turbulent flows, convex optimization

## Abstract

Transient growth and resolvent analyses are routinely used to assess nonasymptotic properties of fluid flows. In particular, resolvent analysis can be interpreted as a special case of viewing flow dynamics as an open system in which free-stream turbulence, surface roughness, and other irregularities provide sources of input forcing. We offer a comprehensive summary of the tools that can be employed to probe the dynamics of fluctuations around a laminar or turbulent base flow in the presence of such stochastic or deterministic input forcing and describe how input–output techniques enhance resolvent analysis. Specifically, physical insights that may remain hidden in the resolvent analysis are gained by detailed examination of input–output responses between spatially localized body forces and selected linear combinations of state variables. This differentiating feature plays a key role in quantifying the importance of different mechanisms for bypass transition in wall-bounded shear flows and in explaining how turbulent jets generate noise. We highlight the utility of a stochastic framework, with white or colored inputs, in addressing a variety of open challenges including transition in complex fluids, flow control, and physics-aware data-driven turbulence modeling. Applications with temporally or spatially periodic base flows are discussed and future research directions are outlined.

**ANNUAL  
REVIEWS** **CONNECT**

[www.annualreviews.org](https://www.annualreviews.org)

- Download figures
- Navigate cited references
- Keyword search
- Explore related articles
- Share via email or social media

## 1. INTRODUCTION

Hydrodynamic stability theory focuses on spectral analysis of the dynamical generator in the linearized Navier–Stokes (NS) equations while seeking the critical Reynolds number at which exponentially growing modes emerge (Schmid & Henningson 2001). Although in many flows predictions agree well with experiments, in wall-bounded shear flows both the critical Reynolds number and the spatial structure of the least-stable or unstable modes are at odds with experimental observations. A broader viewpoint, based on nonmodal analysis of the linearized NS equations, provides reconciliation with experiments and identifies mechanisms for the early stages of subcritical transition (Schmid 2007).

In the words of Trefethen & Embree (2005), the eigenvalue decomposition gives a square matrix, or an operator, a personality. However, this so-called personality test is conclusive only for normal (i.e., unitarily diagonalizable) operators. For nonnormal operators, it is the singular value decomposition (SVD) that offers a robust predictor of personality (Trefethen & Embree 2005). In wall-bounded shear flows, nonnormality of the linearized dynamical operator introduces coupling of exponentially decaying modes, which explains high sensitivity of the laminar flow (Schmid 2007). The high sensitivity degrades the accuracy of analytical and computational predictions that do not explicitly account for modeling imperfections. These are typically difficult to model and may arise from a variety of sources, including surface roughness, thermal fluctuations, and irregularities in the incoming stream.

The study of dynamical systems with input forcing has a rich history in several branches of electrical engineering, including circuit theory, communications, signal processing, and control. In these fields, dynamical systems are decomposed into essential pieces and represented as interconnections of input–output blocks. This input–output viewpoint facilitates the analysis, design, and optimization of complex systems since they can be viewed as simpler subsystems placed in cascade, parallel, and feedback arrangements with one another. It also allows us to quantify the influence of modeling imperfections (e.g., background noise or experimental uncertainty, which is unavoidable in physical systems) on quantities of interest.

In fluid mechanics, input–output analysis addresses the influence of deterministic and stochastic inputs on transient and asymptotic properties of fluid flows. It offers a complementary viewpoint to transient growth (Butler & Farrell 1992) and resolvent (Trefethen et al. 1993) analyses and brings in an appealing robustness interpretation. Specifically, additional insight about the dynamics is gained by carrying out SVD of the operator that maps excitation sources (i.e., inputs such as body-forcing fluctuations) to the quantities of interest (i.e., outputs such as velocity fluctuations). In contrast to the resolvent, this operator is not necessarily a square object; it captures the effect of different inputs to particular physical quantities and thereby reveals finer physical aspects (Jovanović & Bamieh 2005). In wall-bounded shear flows, input–output analysis exposes a large amplification of disturbances and high sensitivity of the laminar flow to uncertainty in the geometry or base velocity (Farrell & Ioannou 1993, Trefethen et al. 1993, Bamieh & Dahleh 2001, Jovanović 2004) and provides insights into structural features of turbulent flows (Hwang & Cossu 2010a,b; McKeon & Sharma 2010). Additional successful applications range from discovering mechanisms for transition to elastic turbulence in viscoelastic fluids (Hoda et al. 2008, 2009; Jovanović & Kumar 2011) to revealing how turbulent jets generate noise (Jeun et al. 2016) and explaining the origin of reattachment streaks in hypersonic flows (Dwivedi et al. 2019).

This review highlights the merits, effectiveness, and versatility of the input–output framework for modeling, analysis, and control of fluid flows. We offer a comprehensive summary of the tools that can be used to probe the dynamics of infinitesimal fluctuations around a given laminar or turbulent base flow and explain how the framework augments resolvent analysis (Trefethen et al.

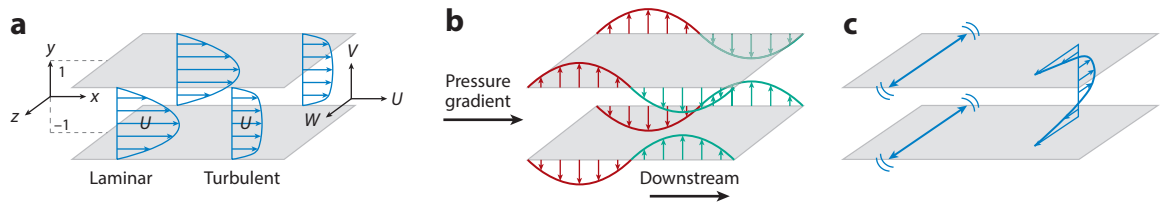


**Figure 1**

A pressure-driven channel flow (a) between two parallel infinite walls with base flow ( $U(y), 0, 0$ ), inhomogeneous wall-normal ( $y$ ), and homogeneous streamwise and spanwise ( $x, z$ ) directions; (b) subject to blowing and suction along the walls; and (c) subject to spanwise wall oscillations.

1993). We illustrate how the componentwise input–output approach (Jovanović & Bamieh 2005) identifies key mechanisms for bypass transition in channel flows of Newtonian and viscoelastic fluids. We then describe how periodic base flow modifications, induced by streamwise traveling waves and spanwise wall oscillations, can be designed to, respectively, control the onset of turbulence (Moarref & Jovanović 2010) and identify the optimal period of oscillation for turbulent drag reduction (Moarref & Jovanović 2012). The input–output framework is also well suited for data-driven turbulence modeling; in contrast to physics-agnostic machine learning techniques, the tools from control theory and convex optimization allow for strategic use of data in order to capture second-order statistics of turbulent flows via first-principle models (Zare et al. 2017b, 2020a).

## 2. INPUT-OUTPUT VIEWPOINT: BEYOND RESOLVENT ANALYSIS

We first review the tools that can be used to probe the dynamics of infinitesimal fluctuations around a given base flow. While this framework can be utilized in a variety of flow regimes and geometries, we resort to a channel flow with homogeneous wall-parallel directions to illustrate the key concepts (see **Figure 1a**). Even in this simple setup, a variety of nontrivial fundamental questions can be addressed by employing an input–output viewpoint, including transition in complex fluids, flow control, and data-driven turbulence modeling.

### 2.1. From the Evolution Model to Input–Output Representation

The linearized NS equations govern the dynamics of infinitesimal fluctuations around a given base flow. Fluctuations can arise from a variety of sources, including surface roughness, imperfections in the incoming stream, acoustics, vibrations, particles, and impurities. In turbulent flows, nonlinear interactions between different length scales can also provide forcing that sustains fluctuations. The linearized NS equations, with an input forcing  $\mathbf{d}_k(t)$  and an output of interest  $\xi_k(t)$ , can be brought to an evolution form (Evolution Model 1):

$$\begin{aligned} \frac{d\psi_k(t)}{dt} &= A_k \psi_k(t) + B_k \mathbf{d}_k(t), \\ \xi_k(t) &= C_k \psi_k(t), \end{aligned} \quad 1.$$

where  $\psi_k(t)$  is the state and  $\mathbf{k}$  is the vector of wave numbers. The operator  $A_k$  characterizes dynamical interactions between the states,  $B_k$  specifies the way the input  $\mathbf{d}_k(t)$  enters into the dynamics, and  $C_k$  maps the state  $\psi_k(t)$  to the output  $\xi_k(t)$ . Equation 1 is a standard state-space model in the controls literature, and it provides a convenient starting point for modal and nonmodal analysis, system identification, turbulence modeling, and flow control.

#### Evolution Model 1:

a first-order differential equation governs the evolution of the state  $\psi_k(t)$ , and a static-in-time equation relates  $\psi_k(t)$  to the output  $\xi_k(t) = C_k \psi_k(t)$ ; apart from the boundary conditions, no additional constraints are imposed on  $\psi_k(t)$

$\mathbf{k}$ : wave numbers

$t$ : time

$A_k$ : dynamical generator

$B_k$ : input operator

$C_k$ : output operator

For a pressure-driven channel flow of an incompressible Newtonian fluid, the base flow  $\bar{\mathbf{u}}$  is given by either the laminar parabolic profile (Poiseuille flow) or the turbulent mean velocity. In both cases, the flow is fully developed and  $\bar{\mathbf{u}}$  only depends on the wall-normal distance,  $y$ :  $\bar{\mathbf{u}} = (U(y), 0, 0)$ . Thus, the linearized NS equations are translationally invariant in wall-parallel directions and in time, and fluctuations can be decomposed in terms of the normal modes in  $x$  and  $z$  as  $\psi(x, y, z, t) = \psi_{\mathbf{k}}(y, t) e^{i(k_x x + k_z z)}$ . Here,  $\mathbf{k} := (k_x, k_z)$  denotes the vector of wall-parallel wave numbers and  $A_{\mathbf{k}}$  is the Orr–Sommerfeld/Squire operator (Schmid & Henningson 2001). In addition to  $\mathbf{k}$ , the system described by Equation 1 is parameterized by the base flow,  $\bar{\mathbf{u}}$ , and the Reynolds number,  $Re$ . For any  $(\mathbf{k}, t)$ , the state,  $\psi_{\mathbf{k}}(t)$ ; input,  $\mathbf{d}_{\mathbf{k}}(t)$ ; and output,  $\xi_{\mathbf{k}}(t)$ , are functions of  $y$ , but for notational convenience we suppress this dependence.

**2.1.1. Derivation of Equation 1.** The linearized model is obtained by expressing the flow as the sum of the base and fluctuation components and by neglecting the quadratic fluctuation terms. In incompressible flows of Newtonian fluids, the velocity obeys a continuity equation, and a Poisson equation for the pressure,  $p$ , is obtained by applying the divergence operator to the linearized NS equations. The Orr–Sommerfeld equation is obtained by acting with the Laplacian,  $\Delta$ , on the wall-normal velocity equation and using the expression for  $\Delta p$  to eliminate  $p$ . The Squire equation is obtained by taking the curl of the linearized NS equations. This yields an evolution model in the form of two partial differential equations for the wall-normal velocity and vorticity (Kim et al. 1987),  $\psi := (v, \eta)$ . All other velocity and vorticity components can be expressed in terms of  $(v, \eta)$  via kinematic relations (Jovanović & Bamieh 2005).

Standard stability analysis of a laminar Poiseuille flow predicts modal instability for  $Re = 5,772$ . The discrepancy with experiments, in which transition occurs for  $Re \approx 1,000$ , can be explained using nonmodal analysis (Schmid 2007), which reveals significant transient growth of fluctuations (Gustavsson 1991, Butler & Farrell 1992) and strong amplification of disturbances (Farrell & Ioannou 1993, Trefethen et al. 1993, Bamieh & Dahleh 2001, Jovanović & Bamieh 2005).

**2.1.2. Resolvent, transfer function, impulse, and frequency response operators.** While the governing equations and geometry determine the dynamical generator,  $A_{\mathbf{k}}$ , there is flexibility in selecting the operators  $B_{\mathbf{k}}$  and  $C_{\mathbf{k}}$ , and different choices can reveal different aspects of flow physics (Jovanović & Bamieh 2005). All of these operators play a role in the response of the system described by Equation 1 that arises from the initial condition  $\psi_{\mathbf{k}}(0)$  and the exogenous input  $\mathbf{d}_{\mathbf{k}}(t)$ :

$$\begin{array}{ccc} \text{Natural response} & \text{Forced response} & \\ \xi_{\mathbf{k}}(t) = & C_{\mathbf{k}} e^{A_{\mathbf{k}} t} \psi_{\mathbf{k}}(0) & + \int_0^t C_{\mathbf{k}} e^{A_{\mathbf{k}}(t-\tau)} B_{\mathbf{k}} \mathbf{d}_{\mathbf{k}}(\tau) d\tau, \end{array} \quad 2.$$

where  $e^{A_{\mathbf{k}} t}$  is the state-transition operator associated with  $A_{\mathbf{k}}$ . The Laplace transform can be utilized to rewrite Equation 2 as

$$\hat{\xi}_{\mathbf{k}}(s) = C_{\mathbf{k}} (sI - A_{\mathbf{k}})^{-1} \psi_{\mathbf{k}}(0) + C_{\mathbf{k}} (sI - A_{\mathbf{k}})^{-1} B_{\mathbf{k}} \hat{\mathbf{d}}_{\mathbf{k}}(s), \quad 3.$$

where  $s$  is the complex number,  $I$  is the identity operator,  $\hat{\xi}_{\mathbf{k}}(s)$  is the Laplace transform of  $\xi_{\mathbf{k}}(t)$ , and  $(sI - A_{\mathbf{k}})^{-1}$  is the resolvent operator. Equations 2 and 3 determine responses of the system described by Equation 1 and provide the basis for quantifying important dynamical features of the linearized flow equations. The natural (i.e., unforced) responses are characterized by the state-transition  $e^{A_{\mathbf{k}} t}$  and resolvent  $(sI - A_{\mathbf{k}})^{-1}$  operators. In contrast, the forced response is obtained by convolving an input  $\mathbf{d}_{\mathbf{k}}(t)$  with the impulse response operator,  $T_{\mathbf{k}}(t)$ ; equivalently, the transfer function  $T_{\mathbf{k}}(s)$  specifies an input–output mapping in the complex domain, i.e.,  $\hat{\xi}_{\mathbf{k}}(s) = T_{\mathbf{k}}(s) \hat{\mathbf{d}}_{\mathbf{k}}(s)$ ,

with

$$\begin{array}{ccc} \text{Impulse response} & & \text{Transfer function} \\ T_{\mathbf{k}}(t) := C_{\mathbf{k}} e^{A_{\mathbf{k}} t} B_{\mathbf{k}} & \xrightarrow{\text{Laplace transform}} & T_{\mathbf{k}}(s) := C_{\mathbf{k}} (sI - A_{\mathbf{k}})^{-1} B_{\mathbf{k}}. \end{array}$$

For flows over perfectly smooth walls and in noise-free environments, study of natural responses aids in understanding the fundamental fluid mechanics. Specifically, the eigenvalue decomposition of  $A_{\mathbf{k}}$  and the SVD of  $e^{A_{\mathbf{k}} t}$ , respectively, offer insights into modal and nonmodal aspects of the flow (Schmid 2007). While such insights are valuable, engineering flows seldom exist in isolation and understanding the forced responses is equally important. In particular, input–output analysis examines forced responses with the objective of quantifying amplification of disturbances and impact of modeling imperfections on fluctuations’ dynamics. In contrast to natural responses, study of forced responses requires specifying how disturbances enter into Equation 1 through the operator  $B_{\mathbf{k}}$ .

In the special case when the input excites all degrees of freedom equally and the output is the entire state,  $B_{\mathbf{k}}$  and  $C_{\mathbf{k}}$  are the identity operators and the resolvent completely determines the transfer function. However, it is often of interest to confine the inputs to certain spatial regions and to examine outputs that are given by a linear combination of certain state variables. In such cases, the transfer function is determined by a compressed resolvent, and its analysis can uncover important dynamical aspects that may be obscured by only paying attention to the standard resolvent. This distinction played a key role in understanding how turbulent jets generate noise. Jeun et al. (2016) utilized compressed resolvent analysis by restricting inputs to the vicinity of the jet turbulence and selecting far-field pressure as the output. In contrast to a standard resolvent analysis, which provides links to jet hydrodynamics but does not explain noise generation (Garnaud et al. 2013), this approach identifies acoustic sources to be wave packets that are in excellent agreement with experiments (Jordan & Colonius 2013) and reveals mechanisms for noise generation.

**2.1.3. Singular value decomposition.** In transient growth analysis, SVD identifies the spatial structure of initial conditions that maximize energy at a given time. SVD also provides the tool for quantifying responses to unsteady deterministic and stochastic inputs,  $\mathbf{d}_{\mathbf{k}}(t)$ , that neither grow nor decay in time (on average). This allows us to set  $s = i\omega$ , and the frequency response,  $T_{\mathbf{k}}(i\omega)$ , is obtained by evaluating the transfer function  $T_{\mathbf{k}}(s)$  along the imaginary axis (see the sidebar titled Frequency Response Operator).

SVD of  $T_{\mathbf{k}}(i\omega)$  identifies fundamental input–output features across  $(\mathbf{k}, \omega)$ :

$$\hat{\xi}_{\mathbf{k}}(i\omega) = T_{\mathbf{k}}(i\omega) \hat{\mathbf{d}}_{\mathbf{k}}(i\omega) = \sum_{j=1}^{\infty} \sigma_{\mathbf{k},j}(\omega) \hat{\mathbf{u}}_{\mathbf{k},j}(\omega) \left\langle \hat{\mathbf{v}}_{\mathbf{k},j}(\omega), \hat{\mathbf{d}}_{\mathbf{k}}(i\omega) \right\rangle. \quad 4.$$

The left and right singular functions,  $\hat{\mathbf{v}}_{\mathbf{k},j}(\omega)$  and  $\hat{\mathbf{u}}_{\mathbf{k},j}(\omega)$ , respectively, provide orthonormal bases of the input and output spaces; the singular value  $\sigma_{\mathbf{k},j}(\omega)$  determines the corresponding amplification; and  $\langle \cdot, \cdot \rangle$  is the inner product. SVD requires computation of the adjoint  $T_{\mathbf{k}}^{\dagger}(i\omega)$ ,

$$\left\langle T_{\mathbf{k}}^{\dagger}(i\omega) \hat{\xi}_{\mathbf{k}}(i\omega), \hat{\mathbf{d}}_{\mathbf{k}}(i\omega) \right\rangle = \left\langle \hat{\xi}_{\mathbf{k}}(i\omega), T_{\mathbf{k}}(i\omega) \hat{\mathbf{d}}_{\mathbf{k}}(i\omega) \right\rangle, \quad 5.$$

and the eigenvalue decomposition of  $TT^{\dagger}$  and  $T^{\dagger}T$ :  $T_{\mathbf{k}}(i\omega)T_{\mathbf{k}}^{\dagger}(i\omega)\hat{\mathbf{u}}_{\mathbf{k},j}(\omega) = \sigma_{\mathbf{k},j}^2(\omega)\hat{\mathbf{u}}_{\mathbf{k},j}(\omega)$  and  $T_{\mathbf{k}}^{\dagger}(i\omega)T_{\mathbf{k}}(i\omega)\hat{\mathbf{v}}_{\mathbf{k},j}(\omega) = \sigma_{\mathbf{k},j}^2(\omega)\hat{\mathbf{v}}_{\mathbf{k},j}(\omega)$ , respectively. Unless noted otherwise, the  $L_2$  inner product  $\langle \cdot, \cdot \rangle$ , which induces an energy norm, is taken over inhomogeneous spatial directions in Equation 4.

---

$C_{\mathbf{k}} e^{A_{\mathbf{k}} t} B_{\mathbf{k}}$ :	impulse response operator
$s = \sigma + i\omega$ :	complex number
$(sI - A_{\mathbf{k}})^{-1}$ :	resolvent operator
$C_{\mathbf{k}}(sI - A_{\mathbf{k}})^{-1} B_{\mathbf{k}}$ :	transfer function
$\omega$ :	frequency
$C_{\mathbf{k}}(i\omega I - A_{\mathbf{k}})^{-1} B_{\mathbf{k}}$ :	frequency response operator
$\mathbb{Z}$ :	set of integers
$\langle \cdot, \cdot \rangle$ :	inner product
$(\cdot)^{\dagger}$ :	adjoint
$L_2$ :	square-integrable function space
$\ \cdot\ $ :	norm
<b>sup</b> :	supremum

---

## FREQUENCY RESPONSE OPERATOR

### Time-Invariant Systems

The natural response of a stable linear time-invariant (LTI) system, described by Equation 1, asymptotically decays to zero. The frequency response operator determines the steady-state response to harmonic inputs with frequency  $\omega$  and is obtained by evaluating the transfer function along the imaginary axis:

$$T_{\mathbf{k}}(i\omega) := T_{\mathbf{k}}(s) \Big|_{s=i\omega} = C_{\mathbf{k}}(i\omega I - A_{\mathbf{k}})^{-1} B_{\mathbf{k}}.$$

For  $\mathbf{d}_{\mathbf{k}}(t) = \hat{\mathbf{d}}_{\mathbf{k}}(i\omega)e^{i\omega t}$ , the steady-state response of a stable LTI system described by Equation 1 is harmonic with the same frequency but with different amplitude and phase, i.e.,  $\xi_{\mathbf{k}}(t) = \hat{\xi}_{\mathbf{k}}(i\omega)e^{i\omega t}$ . The frequency response  $T_{\mathbf{k}}(i\omega)$  is an operator (in inhomogeneous spatial directions) that maps a spatial input profile  $\hat{\mathbf{d}}_{\mathbf{k}}(i\omega)$  into the output  $\hat{\xi}_{\mathbf{k}}(i\omega)$ ,  $\hat{\xi}_{\mathbf{k}}(i\omega) = T_{\mathbf{k}}(i\omega)\hat{\mathbf{d}}_{\mathbf{k}}(i\omega)$ , thereby determining how amplitude and phase change across  $\mathbf{k}$  and  $\omega$ ; see **Figure 2** for an illustration in linearly stable channel flows.

### Time-Periodic Systems

If the operator  $A_{\mathbf{k}}$  in Equation 1 has time-periodic coefficients, i.e.,  $A_{\mathbf{k}}(t) = A_{\mathbf{k}}(t + 2\pi/\omega_t)$ , the steady-state response to a harmonic input with frequency  $\omega$  contains an infinite number of harmonics separated by integer multiples of  $\omega_t$ , i.e.,  $\omega + n\omega_t$ , for  $n \in \mathbb{Z}$ . The proper normal modes for frequency response analysis are no longer purely harmonic ( $e^{i\omega t}$ ). Rather, they are determined by the Bloch waves (Odeh & Keller 1964), i.e., by a product of  $e^{i\theta t}$  and the  $2\pi/\omega_t$ -periodic function in  $t$ :

$$\mathbf{d}_{\mathbf{k}}(t) = \sum_{n=-\infty}^{\infty} \hat{\mathbf{d}}_{\mathbf{k},n}(i\theta) e^{i(\theta + n\omega_t)t}, \quad \theta \in [0, \omega_t),$$

where  $\theta$  is the angular frequency and  $\theta = 0$  and  $\theta = \omega_t/2$  identify the fundamental and subharmonic modes, respectively. The steady-state response of a stable linear time-periodic system to the above Bloch wave input  $\mathbf{d}_{\mathbf{k}}(t)$  is also a Bloch wave,  $\xi_{\mathbf{k}}(t) = \sum_n \hat{\xi}_{\mathbf{k},n}(i\theta) e^{i(\theta + n\omega_t)t}$ , and, for any  $(\mathbf{k}, \theta)$ , the frequency response operator  $T_{\mathbf{k}}(i\theta)$  maps  $\hat{\mathbf{d}}_{\mathbf{k}}(i\theta) := \text{col}\{\hat{\mathbf{d}}_{\mathbf{k},n}(i\theta)\}_{n \in \mathbb{Z}}$  to  $\hat{\xi}_{\mathbf{k}}(i\theta) := \text{col}\{\hat{\xi}_{\mathbf{k},n}(i\theta)\}_{n \in \mathbb{Z}}$ , i.e.,  $\hat{\xi}_{\mathbf{k}}(i\theta) = T_{\mathbf{k}}(i\theta)\hat{\mathbf{d}}_{\mathbf{k}}(i\theta)$ . If the operators  $B_{\mathbf{k}}$  and  $C_{\mathbf{k}}$  in Equation 1 are time invariant, for a system with  $A_{\mathbf{k}}(t) = \sum_m A_{\mathbf{k},m} e^{im\omega_t t}$ , we have

$$T_{\mathbf{k}}(i\theta) = C_{\mathbf{k}}(\mathcal{E}(i\theta) - A_{\mathbf{k}})^{-1} B_{\mathbf{k}},$$

with  $\mathcal{E}(i\theta) := \text{diag}\{i(\theta + n\omega_t)I\}_{n \in \mathbb{Z}}$ , where  $B_{\mathbf{k}}$  and  $C_{\mathbf{k}}$  are the block-diagonal operators with  $B_{\mathbf{k}}$  and  $C_{\mathbf{k}}$  on the main diagonal, respectively, and  $A_{\mathbf{k}} := \text{toep}\{\dots, A_{\mathbf{k},1}, A_{\mathbf{k},0}, A_{\mathbf{k},-1}, \dots\}$  is the block-Toeplitz operator (Jovanović 2008).

## 2.2. Amplification of Deterministic Inputs

For a harmonic input  $\mathbf{d}_{\mathbf{k}}(t) = \hat{\mathbf{d}}_{\mathbf{k}}(i\omega)e^{i\omega t}$  with  $\hat{\mathbf{d}}_{\mathbf{k}}(i\omega) = \hat{\mathbf{v}}_{\mathbf{k},j}(\omega)$ , where  $\hat{\mathbf{v}}_{\mathbf{k},j}(\omega)$  is the  $j$ th left singular function of  $T_{\mathbf{k}}(i\omega)$ , the steady-state output  $\xi_{\mathbf{k}}(t) = \hat{\xi}_{\mathbf{k}}(i\omega)e^{i\omega t}$  of the system described by Equation 1 is in the direction of the  $j$ th right singular function,  $\hat{\xi}_{\mathbf{k}}(i\omega) = \sigma_{\mathbf{k},j}(\omega)\hat{\mathbf{u}}_{\mathbf{k},j}(\omega)$ , and its energy is given by  $\|\hat{\xi}_{\mathbf{k}}(i\omega)\|_2^2 := \langle \hat{\xi}_{\mathbf{k}}(i\omega), \hat{\xi}_{\mathbf{k}}(i\omega) \rangle = \sigma_{\mathbf{k},j}^2(\omega)$ . The principal singular value,  $\sigma_{\mathbf{k},1}(\omega) := \sigma_{\max}(T_{\mathbf{k}}(i\omega))$ , determines the largest amplification at any  $(\mathbf{k}, \omega)$ , and the smallest upper bound over  $\omega$  determines the  $H_{\infty}$  norm of the system described by Equation 1 (Zhou et al. 1996),  $G_{\mathbf{k}} := \sup_{\omega} \sigma_{\mathbf{k},1}(\omega)$ . This measure of input-output amplification has several appealing interpretations for any  $\mathbf{k}$ .



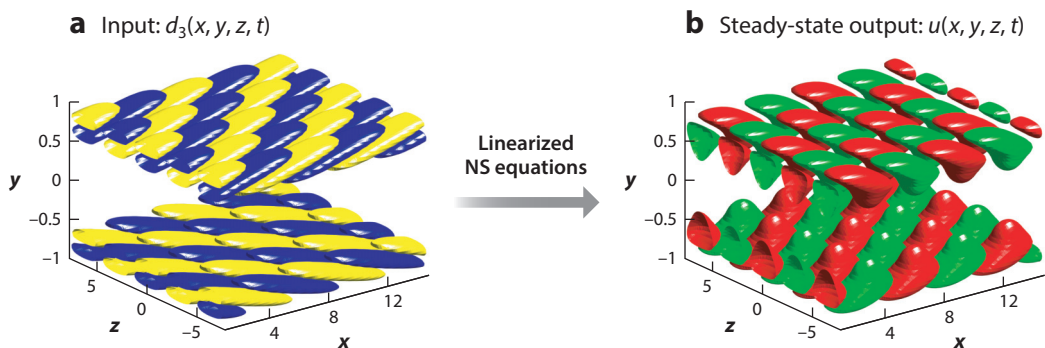


**Figure 2**

In linearly stable channel flows, the steady-state response of the linearized Navier–Stokes (NS) equations to a harmonic input in  $(x, z, t)$ ,  $\hat{\mathbf{d}}_{\mathbf{k}}(y, i\omega) e^{i(k_x x + k_z z + \omega t)}$ , is determined by the output  $\hat{\xi}_{\mathbf{k}}(y, i\omega) e^{i(k_x x + k_z z + \omega t)}$ , with  $\hat{\xi}_{\mathbf{k}}(y, i\omega) = [T_{\mathbf{k}}(i\omega)\hat{\mathbf{d}}_{\mathbf{k}}(\cdot, i\omega)](y)$ , where  $T_{\mathbf{k}}(i\omega)$  is the frequency response operator. (a,b) Spatial structures of (a) spanwise forcing fluctuations and (b) resulting streamwise velocity fluctuations at one time instant in Poiseuille flow with  $Re = 2,000$  for four combinations of  $(k_x, k_z, \omega)$ :  $(1, \pm 1, -0.385)$  and  $(-1, \pm 1, 0.385)$ .

(a) First, the  $H_{\infty}$  norm represents the worst-case amplification of harmonic (in homogeneous directions and in time) deterministic (in inhomogeneous directions) inputs. This worst-case input–output gain is obtained by maximizing over spatial profiles (largest singular value of  $T_{\mathbf{k}}$ ) and temporal frequency (supremum over  $\omega$ ) (see **Figure 3a**). (b) Second, the  $H_{\infty}$  norm determines the induced gain from finite-energy inputs to outputs,  $G_{\mathbf{k}} = \sup_{E_{\mathbf{k}}^{\text{in}} \leq 1} (E_{\mathbf{k}}^{\text{out}}/E_{\mathbf{k}}^{\text{in}})$ , where  $E_{\mathbf{k}}^{\text{in}}$  and  $E_{\mathbf{k}}^{\text{out}}$  denote the  $\mathbf{k}$ -parameterized energy of input and output, e.g.,  $E_{\mathbf{k}}^{\text{in}} := \int_0^{\infty} \|\mathbf{d}_{\mathbf{k}}(t)\|_2^2 dt$ , with  $\|\mathbf{d}_{\mathbf{k}}(t)\|_2^2 = \langle \mathbf{d}_{\mathbf{k}}(t), \mathbf{d}_{\mathbf{k}}(t) \rangle$ . For a unit-energy input  $\mathbf{d}_{\mathbf{k}}(t)$  to the stable system described by Equation 1,  $G_{\mathbf{k}}$  quantifies the largest possible energy of the output  $\xi_{\mathbf{k}}(t)$  across the spatial wave number  $\mathbf{k}$ . (c) Third, the  $H_{\infty}$  norm quantifies robustness to modeling imperfections (see **Figure 3b**).

### 2.3. Amplification of Stochastic Inputs

A common criticism of transient growth and resolvent analyses is the difficulty of implementing the worst-case initial conditions or inputs in the lab. An alternative approach introduces a random

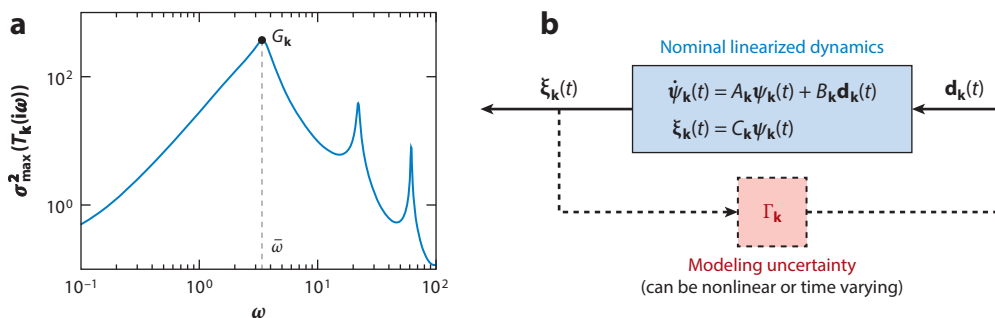


**Figure 3**

(a) The  $H_{\infty}$  norm is determined by the peak value,  $G_{\mathbf{k}}$ , of the largest singular value of the frequency response operator,  $\sigma_{\max}(T_{\mathbf{k}}(i\omega))$ , over the frequency  $\omega$ . (b) A large  $H_{\infty}$  norm of the linearized dynamics signals low robustness margins: Modeling imperfections, captured by the operator  $\Gamma_{\mathbf{k}}$ , with the  $H_{\infty}$  norm  $1/\sqrt{G_{\mathbf{k}}}$  can trigger instability of  $A_{\mathbf{k}} + B_{\mathbf{k}}\Gamma_{\mathbf{k}}C_{\mathbf{k}}$ . This interpretation is related to the pseudo-spectra of linear operators (Trefethen & Embree 2005).

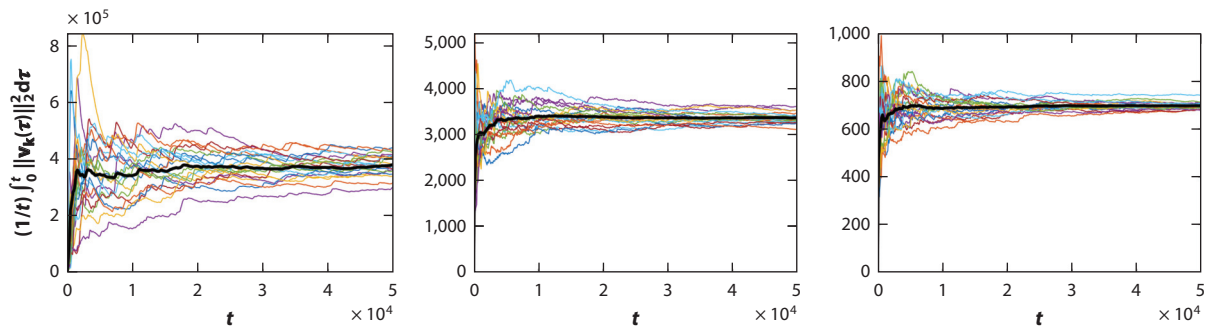


**Figure 4**

The variance of velocity fluctuations,  $(1/t) \int_0^t \|\mathbf{v}_k(\tau)\|_2^2 d\tau$ , for 20 realizations of stochastic forcing to the linearized Navier–Stokes equations in Poiseuille flow with  $Re = 2,000$  for (left to right)  $\mathbf{k} = (0, 1.78)$ ,  $(1, 1)$ , and  $(1, 0)$ . The variance averaged over all simulations is shown by a thick black line.

excitation to the NS equations that can account for background noise. It identifies almost identical dominant flow structures and opens the door to turbulence modeling.

Control-theoretic tools can be utilized to exploit the structure of the linearized Equation 1, avoid costly stochastic simulations, and offer insight into amplification mechanisms. For 20 realizations of persistent channel-wide temporally and spatially uncorrelated stochastic input  $\mathbf{d}_k(t)$  to Equation 1, **Figure 4** shows the variance of the velocity fluctuation vector  $\mathbf{v}_k(t) := (u_k(t), v_k(t), w_k(t))$  in Poiseuille flow with  $Re = 2,000$ . Although individual simulations display different responses, their average reaches the steady-state limit. In the absence of modal instability, viscosity asymptotically dissipates natural responses but a persistent excitation source maintains fluctuations for all times.

**2.3.1. The Reynolds–Orr equation.** In channel flow with stochastic forcing, the kinetic energy  $E_k(t) := \mathbf{E}(\langle \mathbf{v}_k(t), \mathbf{v}_k(t) \rangle)$  of fluctuations  $\mathbf{v}_k(t)$  around  $(U(y), 0, 0)$  obeys

$$\frac{1}{2} \frac{dE_k(t)}{dt} = \mathbf{E} \left[ \frac{1}{Re} \langle \mathbf{v}_k(t), \Delta \mathbf{v}_k(t) \rangle - \langle u_k(t), U' v_k(t) \rangle + \langle \mathbf{v}_k(t), \mathbf{d}_k(t) \rangle \right].$$

Here,  $\mathbf{E}$  is the expectation operator,  $\langle \cdot, \cdot \rangle$  is the  $L_2[-1, 1]$  inner product,  $U'(y)$  is defined as  $dU(y)/dy$ , and the terms on the right-hand side denote the viscous energy dissipation, the energy exchange with the base shear, and the work done by the body forces, respectively. The nonlinear terms in the NS equations are conservative and the Reynolds–Orr equation takes the same form for nonlinear and linearized dynamics (Schmid & Henningson 2001). Since it is driven by the terms that need to be determined by solving the equations for flow fluctuations, it is not in the form that allows for direct determination of its solution. For the linearized NS equations, both the kinetic energy and the terms on the right-hand side of the Reynolds–Orr equation can be computed using the solution to the differential Lyapunov equation (Equation 6), which we present below. This avoids the need for costly stochastic simulations and provides an alternative way of solving an important equation in fluid mechanics.

**2.3.2. Time-invariant systems.** Let the system described by Equation 1, with the output  $\xi_k(t) = \mathbf{v}_k(t)$ , be driven by a stochastic input  $\mathbf{d}_k(t)$  with the spectral density  $\Omega_k(i\omega)$ . The spectral density operator,  $S_k(i\omega) = T_k(i\omega)\Omega_k(i\omega)T_k^\dagger(i\omega)$ , quantifies the two-point correlations of  $\mathbf{v}_k(t)$  across the wave number  $\mathbf{k}$  and the frequency  $\omega$ , where  $T_k(i\omega)$  is the frequency response operator defined in the sidebar titled Frequency Response Operator. The inverse Fourier transform of

$\mathbf{E}(\cdot)$ : expectation operator



$S_k(i\omega)$  yields the lagged covariance operator,

$$R_k(\tau) := \lim_{t \rightarrow \infty} \mathbf{E}[\mathbf{v}_k(t) \otimes \mathbf{v}_k(t + \tau)] = \frac{1}{2\pi} \int_{-\infty}^{+\infty} S_k(i\omega) e^{i\omega\tau} d\omega,$$

where  $\otimes$  denotes the tensor product. Furthermore, the integration of  $S_k(i\omega)$  over  $\omega$  yields the steady-state two-point correlation (i.e., covariance) operator  $V_k$  of the output  $\mathbf{v}_k(t)$ ,

$$V_k := R_k(0) = \lim_{t \rightarrow \infty} V_k(t) = \frac{1}{2\pi} \int_{-\infty}^{+\infty} S_k(i\omega) d\omega,$$

where  $V_k(t) := \mathbf{E}[\mathbf{v}_k(t) \otimes \mathbf{v}_k(t)]$  is the time-dependent covariance operator of velocity fluctuations. For the system described by Equation 1, we have  $V_k(t) = C_k X_k(t) C_k^\dagger$ , where  $X_k(t) := \mathbf{E}[\Psi_k(t) \otimes \Psi_k(t)]$  is the covariance operator of the state  $\Psi_k(t)$  and  $C_k^\dagger$  is the adjoint of the operator  $C_k$ . In channel flow, for any  $\mathbf{k}$ ,  $V_k$  is an operator in the wall-normal direction,  $\mathbf{g}_k(y_1) := [V_k \mathbf{f}_k(\cdot)](y_1)$ , whose kernel representation determines all stationary two-point correlations of  $\mathbf{v}_k(t)$ :

$$\mathbf{g}_k(y_1) = \int_{-1}^1 V_k^{\text{ker}}(y_1, y_2) \mathbf{f}_k(y_2) dy_2 = \int_{-1}^1 \lim_{t \rightarrow \infty} \mathbf{E}[\mathbf{v}_k(y_1, t) \mathbf{v}_k^*(y_2, t)] \mathbf{f}_k(y_2) dy_2.$$

One- and two-point correlations in  $y$  are obtained for  $y_1 = y_2$  and  $y_1 \neq y_2$ , respectively;  $V_k^{\text{ker}}(y_1, y_2)$  determines the two-point spectral density tensor and its inverse Fourier transform gives the two-point correlation tensor in  $x$  and  $z$  (Moin & Moser 1989).

**2.3.3. Lyapunov equation.** For a zero-mean temporally uncorrelated input  $\mathbf{d}_k(t)$  with the covariance operator  $W_k$ , i.e.,  $\mathbf{E}[\mathbf{d}_k(t)] = 0$ ,  $\mathbf{E}[\mathbf{d}_k(t) \otimes \mathbf{d}_k(\tau)] = W_k \delta(t - \tau)$ , the input spectral density,  $\Omega_k(i\omega)$ , is constant across  $\omega$ , i.e.,  $\Omega_k(i\omega) = W_k$ . In this case, as described in the sidebar titled Lyapunov Equation, the covariance operator  $X_k(t)$  of the state  $\Psi_k(t)$  in Equation 1 satisfies the differential Lyapunov equation:

$$\frac{dX_k(t)}{dt} = A_k X_k(t) + X_k(t) A_k^\dagger + B_k W_k B_k^\dagger. \quad 6.$$

For the system described by Equation 1 with the input covariance  $W_k$  and the initial condition  $X_k(0)$ , this operator-valued differential equation can be used to compute  $X_k(t)$  and determine energy of fluctuations via  $E_k(t) = \text{trace}[C_k X_k(t) C_k^\dagger]$ . For linearly unstable flows, the steady-state limit of  $X_k(t)$  either is unbounded or does not exist. However, the solution of Equation 6 can still be computed, e.g., by forward-marching in time or via the following formula:

$$X_k(t) = e^{A_k t} X_k(0) e^{A_k^\dagger t} + \left[ \begin{array}{cc} I & 0 \end{array} \right] \exp \left( \left[ \begin{array}{cc} A_k & B_k W_k B_k^\dagger \\ 0 & -A_k^\dagger \end{array} \right] t \right) \left[ \begin{array}{c} 0 \\ I \end{array} \right] e^{A_k^\dagger t}.$$

In the absence of modal instability,  $X_k := \lim_{t \rightarrow \infty} X_k(t)$  is well defined and the steady-state limit of Equation 6 is given by

$$A_k X_k + X_k A_k^\dagger = -B_k W_k B_k^\dagger. \quad 7.$$

In this case, for a given initial condition  $X_k(0)$ ,  $X_k(t)$  can be computed from the solution  $X_k$  to the algebraic Lyapunov equation (Equation 7) via  $X_k(t) = X_k - e^{A_k t} [X_k - X_k(0)] e^{A_k^\dagger t}$ , and the steady-state limit of  $E_k(t)$  determines the energy amplification  $E_k := \lim_{t \rightarrow \infty} E_k(t) = \text{trace}(C_k X_k C_k^\dagger)$  (see the sidebar titled Power Spectral Density and Energy Amplification). Finally, for colored-in-time input  $\mathbf{d}_k(t)$ ,  $X_k$  satisfies

$$A_k X_k + X_k A_k^\dagger = -(B_k H_k^\dagger + H_k B_k^\dagger), \quad 8.$$

where the operator  $H_k$  determines the stationary cross-correlation between the input  $\mathbf{d}_k(t)$  and the state  $\Psi_k(t)$  in Equation 1 (Zare et al. 2017b, appendix B).

$[\mathbf{u} \otimes \mathbf{v}] \mathbf{w} := \mathbf{u} \langle \mathbf{v}, \mathbf{w} \rangle$ :  
tensor product

$(\cdot)^*$ :  
complex-conjugate  
transpose

## LYAPUNOV EQUATION: TWO-POINT CORRELATIONS OF LINEAR SYSTEMS

The Lyapunov equation can be used to propagate two-point correlations of the white stochastic input  $\mathbf{d}(t)$  into colored statistics of the state  $\boldsymbol{\psi}(t)$  of a linear system (Bamieh & Dahleh 2001, appendix A). Here we derive the Lyapunov equation for a finite-dimensional discrete-time LTI system (DT LTI):

$$\boldsymbol{\psi}(t+1) = A\boldsymbol{\psi}(t) + B\mathbf{d}(t),$$

where time  $t$  is a nonnegative integer and  $A, B$  are constant matrices. The derivation for continuous-time systems is standard (Kwakernaak & Sivan 1972, chapter 1.11) but is more involved and less intuitive. Let  $X(t) := \mathbf{E}[\boldsymbol{\psi}(t)\boldsymbol{\psi}^*(t)]$  be the covariance matrix of the state at time  $t$ , where  $\mathbf{E}$  is the expectation operator and  $\boldsymbol{\psi}^*(t)$  is the complex-conjugate transpose of  $\boldsymbol{\psi}(t)$ . Then the DT LTI can be used to obtain the following recursion:

$$\begin{aligned} X(t+1) &= \mathbf{E} \{ [A\boldsymbol{\psi}(t) + B\mathbf{d}(t)] [\boldsymbol{\psi}^*(t)A^* + \mathbf{d}^*(t)B^*] \} \\ &= A\mathbf{E}[\boldsymbol{\psi}(t)\boldsymbol{\psi}^*(t)]A^* + B\mathbf{E}[\mathbf{d}(t)\boldsymbol{\psi}^*(t)]A^* + A\mathbf{E}[\boldsymbol{\psi}(t)\mathbf{d}^*(t)]B^* + B\mathbf{E}[\mathbf{d}(t)\mathbf{d}^*(t)]B^*. \end{aligned}$$

If the stochastic input is white-in-time with the covariance matrix  $W$ , i.e.,  $\mathbf{E}[\mathbf{d}(t)\mathbf{d}^*(\tau)] = W\delta(t - \tau)$ , where  $\delta$  is the Kronecker delta, the cross terms in the above recursion disappear and we obtain the Lyapunov equation:

$$X(t+1) = AX(t)A^* + BWB^*, \quad X(0) = X_0.$$

If the matrices  $A$  and  $B$  in the DT LTI as well as the matrices  $W$  and  $X_0$  are known, this deterministic equation can be propagated forward in time to obtain the covariance matrix  $X(t)$ . Even though the above derivation holds irrespective of stability properties of the DT LTI system, the steady-state limit,  $X := \lim_{t \rightarrow \infty} X(t)$ , only exists for stable systems. In this case, the Lyapunov equation converges to the algebraic Lyapunov equation,

$$AXA^* - X = -BWB^*,$$

which is linear in  $X$  and is typically used to compute the stationary covariance matrix  $X$  for given  $A, B$ , and  $W$ . For colored-in-time stochastic inputs  $\mathbf{d}(t)$ , the cross terms in the above recursion are nonzero and introducing the matrix  $H(t) := A\mathbf{E}[\boldsymbol{\psi}(t)\mathbf{d}^*(t)] + \frac{1}{2}B\mathbf{E}[\mathbf{d}(t)\mathbf{d}^*(t)]$  in the recursion allows us to write it as

$$X(t+1) = AX(t)A^* + BH^*(t) + H(t)B^*, \quad X(0) = X_0,$$

which, for the stable DT LTI system, converges asymptotically to the algebraic Lyapunov-like equation,

$$AXA^* - X = -(BH^* + HB^*),$$

with  $H := \lim_{t \rightarrow \infty} H(t)$ . For continuous-time systems, the Lyapunov equation above takes the form of the differential Lyapunov equation (Equation 6), which, for stable systems, converges to the algebraic Lyapunov equation (Equation 7). While the above equations also hold for systems in which  $A(t)$  and  $B(t)$  depend on time, their steady-state limits may not be well defined. Finally, for infinite-dimensional systems, the complex-conjugate transpose of a matrix,  $A^*$ , should be replaced with an adjoint of an operator,  $A^\dagger$ .

Departure from the white-in-time restriction removes the sign-definiteness requirement on the right-hand side in Equation 7: While the operator  $B_k W_k B_k^\dagger$  in Equation 7 has nonnegative eigenvalues,  $B_k H_k^\dagger + H_k B_k^\dagger$  in Equation 8 is allowed to be sign indefinite, which provides additional flexibility. Furthermore, for a zero-mean white input  $\mathbf{w}_k(t)$  with the covariance operator  $W_k$ , the stationary covariance operator of  $\boldsymbol{\psi}_k(t)$  in the system

$$\frac{d}{dt} \begin{bmatrix} \boldsymbol{\psi}_k(t) \\ \boldsymbol{\phi}_k(t) \end{bmatrix} = \begin{bmatrix} A_k & -B_k K_k \\ 0 & A_k - B_k K_k \end{bmatrix} \begin{bmatrix} \boldsymbol{\psi}_k(t) \\ \boldsymbol{\phi}_k(t) \end{bmatrix} + \begin{bmatrix} B_k \\ B_k \end{bmatrix} \mathbf{w}_k(t), \quad 9.$$

## POWER SPECTRAL DENSITY AND ENERGY AMPLIFICATION

The power spectral density quantifies the energy of the output  $\mathbf{x}_k(t)$  of the stochastically forced system described by Equation 1 across the wave number  $\mathbf{k}$  and temporal frequency  $\omega$ :

$$\Pi_k(\omega) := \text{trace} [S_k(i\omega)] = \text{trace} [T_k(i\omega)\Omega_k(i\omega)T_k^\dagger(i\omega)],$$

where  $T_k(i\omega)$  is the frequency response and  $\Omega_k(i\omega)$  is the spectral density of  $\mathbf{d}_k(t)$ . At any  $\mathbf{k}$ , the temporal average of  $\Pi_k(\omega)$  determines the energy (variance) amplification of harmonic (in homogeneous spatial directions) stochastic (in inhomogeneous directions and time) disturbances to the linearized NS equations:

$$E_k := \frac{1}{2\pi} \int_{-\infty}^{\infty} \Pi_k(\omega) d\omega.$$

This quantity is also known as the ensemble-average energy density of the statistical steady state, and it is hereafter referred to as the (steady-state) energy amplification (or energy density). For white-in-time inputs  $\mathbf{d}_k(t)$  with  $\Omega_k(i\omega) = W_k$ , the solution to the algebraic Lyapunov equation (Equation 7) can be used to compute  $E_k$ :

$$E_k = \text{trace} (C_k X_k C_k^\dagger), \quad \text{EA.}$$

thereby avoiding integration over  $\omega$ . When the input is uncorrelated in inhomogeneous spatial directions with  $W_k = I$ , the sum of squares of the singular values of  $T_k(i\omega)$  gives the power spectral density, i.e., the Hilbert–Schmidt norm of  $T_k(i\omega)$ . In this case,  $E_k$  determines the  $H_2$  norm of the system described by Equation 1 and Parseval’s identity yields

$$E_k = \frac{1}{2\pi} \int_{-\infty}^{\infty} \sum_{j=1}^{\infty} \sigma_{k,j}^2(\omega) d\omega = \frac{1}{2\pi} \int_{-\infty}^{\infty} \text{trace} [T_k(i\omega)T_k^\dagger(i\omega)] d\omega = \int_{-\infty}^{\infty} \text{trace} [T_k(t)T_k^\dagger(t)] dt.$$

Thus, in addition to quantifying the steady-state variance of the system described by Equation 1 subject to spatially and temporally uncorrelated stochastic inputs, the  $H_2$  norm also determines the  $L_2$  norm of the impulse response and the same control-theoretic quantity enjoys both stochastic and deterministic interpretations.

### Comparison of $H_2$ and $H_\infty$ norms

For flows without homogeneous directions, the  $H_2$  and  $H_\infty$  norms compress the dynamics into a single positive number; otherwise, they are parameterized by the wave number,  $\mathbf{k}$ . Section 2.2 offers interpretations of the  $H_\infty$  norm and this sidebar discusses the  $H_2$  norm. Here we highlight how these measures of input–output amplification of the system described by Equation 1 compress information in inhomogeneous directions and in time: While the  $H_\infty$  norm maximizes over both spatial profiles and frequency by computing the temporal supremum of  $\sigma_{\max} [T_k(i\omega)]$ , the  $H_2$  norm quantifies the aggregate effect of inputs by integrating the sum of squares of the singular values of  $T_k(i\omega)$  over  $\omega$ .

with  $K_k := [(1/2)W_k B_k^\dagger - H_k^\dagger]X_k^{-1}$ , is given by  $X_k$  (Zare et al. 2017b). The  $\phi_k$  subsystem in Equation 9 maps the white input  $\mathbf{w}_k(t)$  to the colored input  $\mathbf{d}_k(t)$  in the system described by Equation 1 such that we have  $X_k = \lim_{t \rightarrow \infty} \mathbf{E} [\psi_k(t) \otimes \psi_k(t)]$ . Equivalently, the mapping from  $\mathbf{w}_k(t)$  to  $\psi_k(t)$  in Equation 9 can be represented via

$$\frac{d\psi_k(t)}{dt} = (A_k - B_k K_k) \psi_k(t) + B_k \mathbf{w}_k(t), \quad 10.$$

and the algebraic Lyapunov equation (Equation 7) can be used to verify that the stationary two-point correlation operator of  $\psi_k(t)$  is indeed given by  $X_k$ . Thus, the impact of a colored-in-time input can be interpreted as a state-feedback modification of the operator  $A_k$  in Equation 1.

For a stable stochastically forced system described by Equation 1, Equation 8 identifies admissible steady-state covariance operators. This fundamental relation was recently utilized for low-complexity stochastic dynamical modeling of turbulent flows (Zare et al. 2017a,b, 2020a).

**2.3.4. Time-periodic systems.** The response of a linear time-periodic system to a stationary stochastic input is a cyclo-stationary process (Gardner 1990); the covariance operator of the state is  $2\pi/\omega_t$  periodic, i.e.,  $X_{\mathbf{k}}(t) := \mathbf{E}[\psi_{\mathbf{k}}(t) \otimes \psi_{\mathbf{k}}(t)] = \sum_n X_{\mathbf{k},n} e^{in\omega_t t}$ , with  $X_{\mathbf{k},-n} = X_{\mathbf{k},n}^\dagger$ , and the effect of the stationary input, over one period  $T := 2\pi/\omega_t$ , is determined by  $(1/T) \int_0^T X_{\mathbf{k}}(t) dt = X_{\mathbf{k},0}$ . If the stochastic input  $\mathbf{d}_{\mathbf{k}}(t)$  is white-in-time with the spatial covariance  $W_{\mathbf{k}}$ , the harmonic Lyapunov equation,

$$[A_{\mathbf{k}} - \mathcal{E}(i0)]\mathcal{X}_{\mathbf{k}} + \mathcal{X}_{\mathbf{k}}[A_{\mathbf{k}} - \mathcal{E}(i0)]^\dagger = -B_{\mathbf{k}}W_{\mathbf{k}}B_{\mathbf{k}}^\dagger, \quad 11.$$

can be used to compute the Fourier series coefficients  $X_{\mathbf{k},n}$  of  $X_{\mathbf{k}}(t)$ . Here,  $A_{\mathbf{k}}$ ,  $B_{\mathbf{k}}$ , and  $\mathcal{E}$  are defined in the sidebar titled Frequency Response Operator;  $W_{\mathbf{k}}$  is the block-diagonal operator with  $W_{\mathbf{k}}$  on the main diagonal; and  $\mathcal{X}_{\mathbf{k}}$  is the self-adjoint block-Toeplitz operator whose elements are determined by  $X_{\mathbf{k},n}$  (Jovanović 2008, Jovanović & Fardad 2008).

### 3. UNCOVERING MECHANISMS IN WALL-BOUNDED SHEAR FLOWS

We next illustrate how the input–output approach provides insights into the physics of transitional and turbulent wall-bounded shear flows of Newtonian and viscoelastic fluids. In addition to offering a computational framework that quantifies the impact of modeling imperfections on relevant flow quantities, a control-theoretic viewpoint also reveals influence of dimensionless groups on amplification of deterministic as well as stochastic disturbances and uncovers mechanisms that may initiate bypass transition. In Section 3.1, we highlight how streamwise streaks, oblique waves, and Orr–Sommerfeld modes are identified as input–output resonances of the operator that maps forcing fluctuations to different velocity components in Newtonian fluids. In Section 3.2, we demonstrate how a control-theoretic approach reveals a viscoelastic analog of the familiar inertial lift-up mechanism, thereby identifying mechanisms that may trigger transition to elastic turbulence in rectilinear flows of viscoelastic fluids. Finally, in Section 3.3, we offer a brief overview of the merits and the effectiveness of the input–output analysis in turbulent channel and pipe flows of Newtonian fluids.

#### 3.1. Bypass Transition in Channel Flows of Newtonian Fluids

For Poiseuille flow with  $Re = 2,000$ , **Figure 4** shows that the streamwise-constant flow structures with  $k_z = 1.78$  are much more energetic than the oblique waves ( $k_x = k_z = 1$ ) and the Orr–Sommerfeld modes ( $k_x = 1, k_z = 0$ ). We next illustrate how the tools of Section 2.3 offer insights into the physics of transitional flows while avoiding need for stochastic simulations. **Figure 5** displays the joint impact of forcing fluctuations in all three spatial directions on the individual velocity components. For a channel-wide forcing  $\mathbf{d}_{\mathbf{k}}(t)$ , we utilize the expression for the energy amplification in the sidebar titled Power Spectral Density and Energy Amplification to evaluate the impact of the wave numbers  $k_x$  and  $k_z$  on the steady-state variance of  $u$ ,  $v$ , and  $w$ . The streamwise velocity component,  $u$ , contains most energy, and the strongest amplification occurs in the region that corresponds to small values of  $k_x$  and  $\mathcal{O}(1)$  values of  $k_z$ . The oblique modes [i.e., the flow structures with  $\mathcal{O}(1)$  values of  $k_x$  and  $k_z$ ] emerge as input–output resonances in the response of the spanwise velocity,  $w$ , and they are significantly less amplified than the streamwise-elongated flow structures with  $k_x \approx 0$ . In contrast, the least-stable Orr–Sommerfeld mode, which is the

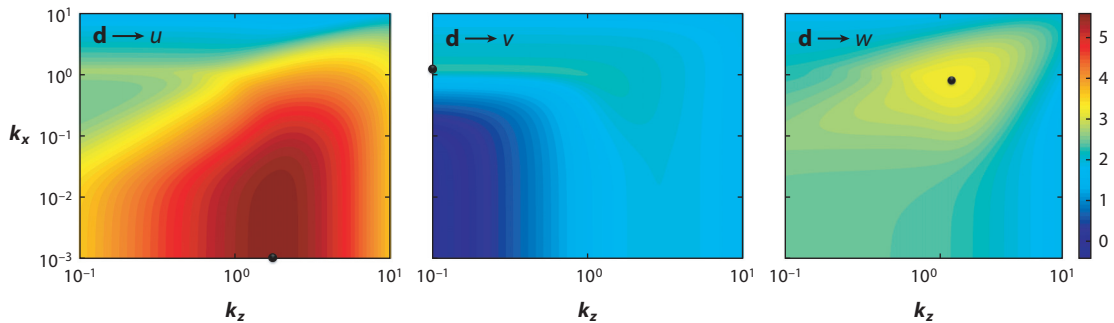


**Figure 5**

Energy amplification of (left to right) streamwise ( $u$ ), wall-normal ( $v$ ), and spanwise ( $w$ ) velocity fluctuations for the linearized Navier–Stokes equations subject to channel-wide stochastic forcing in Poiseuille flow with  $Re = 2,000$ . The largest value in each plot is marked by a black dot and a logarithmic scaling with the same color map is employed. The streamwise velocity contains most energy and the dominant flow structures are given by the streamwise-elongated spanwise-periodic streaks.

dominant source of amplification for the wall-normal velocity,  $v$ , creates only a local peak around ( $k_x \approx 1, k_z = 0$ ) in the response of  $u$ . Thus, the flow structures that are deemed important in classical hydrodynamic stability play a marginal role in the amplification of stochastic disturbances. This identifies shortcomings of modal stability theory, highlights the utility of componentwise input–output analysis (Jovanović & Bamieh 2005), and demonstrates that significant insight can be gained by examining linearized dynamics in the presence of modeling imperfections (in this case, additive stochastic disturbances).

**3.1.1. Streamwise-constant model: lift-up mechanism.** In addition to computational advantages, a control-theoretic viewpoint also uncovers mechanisms for subcritical transition and quantifies impact of the Reynolds number on amplification of deterministic as well as stochastic disturbances (Jovanović 2004, Jovanović & Bamieh 2005). By considering how the disturbances propagate through the linearized dynamics, important insight can be gained without any computations. Since the streamwise-constant fluctuations experience the largest amplification (see **Figure 5**), we examine the system described by the linearized dimensionless NS equations for  $\mathbf{k} := (k_x, k_z) = (0, k_z)$ :

$$\begin{aligned} \frac{d}{dt} \begin{bmatrix} v(t) \\ \eta(t) \end{bmatrix} &= \overbrace{\begin{bmatrix} \frac{1}{Re} A_{os} & 0 \\ A_{cp1} & \frac{1}{Re} A_{sq} \end{bmatrix}}^{\text{Nonnormal}} \begin{bmatrix} v(t) \\ \eta(t) \end{bmatrix} + \begin{bmatrix} 0 & B_2 & B_3 \\ B_1 & 0 & 0 \end{bmatrix} \begin{bmatrix} d_1(t) \\ d_2(t) \\ d_3(t) \end{bmatrix}, \\ \begin{bmatrix} u(t) \\ v(t) \\ w(t) \end{bmatrix} &= \begin{bmatrix} 0 & C_u \\ C_v & 0 \\ C_w & 0 \end{bmatrix} \begin{bmatrix} v(t) \\ \eta(t) \end{bmatrix}, \end{aligned} \quad 12.$$

where we suppress the dependence on the spanwise wave number,  $k_z$ . Here,  $v$  and  $\eta$  respectively denote the wall-normal velocity and vorticity fluctuations, whereas  $(d_1, d_2, d_3)$  and  $(u, v, w)$  are respectively the forcing and velocity fluctuations in  $(x, y, z)$ . The Orr–Sommerfeld, Squire, and coupling operators are given by  $A_{os} := \Delta^{-1} \Delta^2$ ,  $A_{sq} := \Delta$ , and  $A_{cp1} := -ik_z U'(y)$ , respectively, where  $\Delta = \partial_{yy} - k_z^2 I$  is a Laplacian with homogeneous Dirichlet boundary conditions,  $\Delta^{-1}$  is the inverse of the Laplacian,  $\Delta^2$  is defined as  $\partial_{yyy} - 2k_z^2 \partial_{yy} + k_z^4 I$  with homogeneous Dirichlet and Neumann boundary conditions, and  $U'(y)$  is again  $dU(y)/dy$ . We refer the reader to section 4 of Jovanović & Bamieh (2005) for a definition of the input,  $B$ , and output,  $C$ , operators.

#### Dimensionless NS equations:

in incompressible Newtonian fluids with density  $\rho$ , we scale length with the channel half-height  $b$ , velocity with  $\bar{u}$ , time with the inertial timescale  $b/\bar{u}$ , pressure with  $\rho \bar{u}^2$ , and forcing per unit mass with  $\bar{u}^2/b$ ; in analysis of transition,  $\bar{u}$  is the largest velocity of the laminar base flow and, in analysis of turbulence,  $\bar{u}$  is the friction velocity

## BLOCK DIAGRAMS: A TOOL FOR REVEALING STRUCTURE WITHOUT COMPUTATIONS

Block diagrams decompose complex systems into essential pieces, abstract away unnecessary details, and highlight the flow of information. These control-theoretic tools reveal structure without any computations and allow one to make useful analogies. Circles are used to denote the summation of input signals and boxes represent different parts of the system. Inputs into each box/circle are represented by lines with arrows directed toward the box/circle, and outputs are represented by lines with arrows leading away from the box/circle. The inputs specify the signals affecting subsystems, and the outputs specify the signals of interest or signals affecting other parts of the system. The block diagrams in **Figure 6** illustrate influence of disturbances  $d_1$ ,  $d_2$ , and  $d_3$  to the momentum equation on the velocity fluctuations  $u$ ,  $v$ , and  $w$  in streamwise-constant channel flows of Newtonian and inertialess viscoelastic fluids.

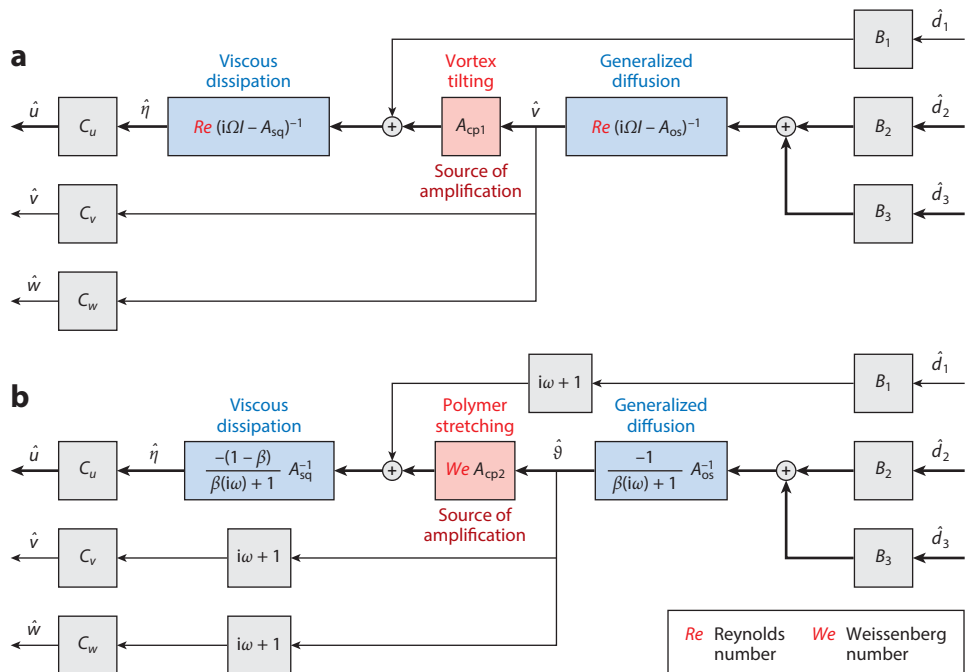


**Figure 6**

Block diagrams of the frequency response operators that map the forcing fluctuations  $d_1$ ,  $d_2$ , and  $d_3$  to the velocity fluctuations  $u$ ,  $v$ , and  $w$  in streamwise-constant channel flows of (a) Newtonian fluids and (b) inertialess Oldroyd-B fluids. Blue boxes represent resolvent operators associated with the Orr–Sommerfeld,  $A_{os}$ , and Squire,  $A_{sq}$ , operators, and red boxes represent the coupling operators  $A_{cp1} := -ik_z U'(y)$  and  $A_{cp2} := ik_z [U'(y)\Delta + 2U''(y)\partial_y]$ . In Newtonian fluids,  $\Omega := \omega Re$  is the frequency scaled with the diffusive timescale,  $b^2/\nu$ , and in viscoelastic fluids,  $\omega$  is the frequency scaled with the polymer relaxation time,  $\lambda$ . The thick black lines indicate the part of the system responsible for large amplification. In Newtonian fluids, amplification originates from vortex tilting, i.e., the operator  $A_{cp1}$  in Equation 12, and in viscoelastic fluids, it originates from polymer stretching, i.e., the operator  $A_{cp2}$ . In Newtonian fluids, singular values of the frequency responses from  $d_l$  to  $r$  are proportional to  $Re^2$  for  $r = u$  and  $l = \{2, 3\}$ ; are proportional to  $Re$  for  $\{r = u, l = 1; r = \{v, w\}, l = \{2, 3\}\}$ ; and are equal to zero for  $\{r = \{v, w\}, l = 1\}$ . In inertialess flows of viscoelastic fluids, they are proportional to  $We$  for  $\{r = u, l = \{2, 3\}\}$ ; all other singular values are independent of  $We$ .



As described in the sidebar titled Block Diagrams, block diagrams are control-theoretic tools that decompose complex systems into essential pieces, abstract away unnecessary details, and highlight the flow of information. A graphical representation of the frequency response operator in **Figure 6a** illustrates that the wall-normal and spanwise forcing fluctuations,  $d_2$  and  $d_3$ , produce  $\mathcal{O}(Re)$  fluctuations in  $v$  and  $w$ , respectively. Although these are dissipated by viscosity, the resulting spanwise variations in  $v$ ,  $ik_z v$ , tilt the spanwise vorticity of the laminar base flow,  $-U'(y)$ , in the wall-normal direction,  $y$ , thereby triggering  $\mathcal{O}(Re^2)$  fluctuations in  $\eta$  and, consequently, in  $u = \eta/(ik_z)$ . This lift-up mechanism (Landahl 1975) is a dominant source of amplification in wall-bounded shear flows of Newtonian fluids. The operator  $\mathcal{A}_{cp1}$  acts as a source in the wall-normal vorticity equation and accounts for vortex tilting that arises from linearization of the convective terms in the NS equations. Since the operators  $\mathcal{A}_{os}$  and  $\mathcal{A}_{sq}$  are self-adjoint, in the absence of vortex tilting, the dynamics are characterized by viscous dissipation.

### 3.2. Early Stages of Transition to Elastic Turbulence: Viscoelastic Lift-Up

In complex fluids and complex flows, it is even more important to explicitly account for modeling imperfections by quantifying their influence on transient and asymptotic dynamics. Here we illustrate how input–output analysis discovers mechanisms that may initiate bypass transition in channel flows of viscoelastic fluids in the absence of inertia. Transition in fluids that contain polymer chains can impact polymer processing and enhance microfluidic mixing. In contrast to Newtonian fluids, viscoelastic liquids can deviate from laminar profiles even when inertia is negligible (Groisman & Steinberg 2000), and in curvilinear flows, a purely elastic instability triggers transition (Larson et al. 1990). In low-inertial regimes, rectilinear flows are asymptotically stable but the dynamics associated with polymer stress fluctuations can still induce complex responses (Qin et al. 2019a,b). Since no single constitutive equation fully describes the range of phenomena in viscoelastic fluids, it is important to understand how modeling imperfections may adversely affect their dynamics.

Newtonian fluids are characterized by a static-in-time linear relation between stresses and velocity gradients. In viscoelastic fluids, constitutive equations determine the influence of velocity gradients on the dynamics of the stress tensor. For dilute polymer solutions, polymer molecules are treated as springs that connect spherical beads (Bird et al. 1987); the Oldroyd-B (infinitely extensible linear spring) and the FENE (finitely extensible nonlinear elastic)-type models are most commonly used. In the absence of inertia, we can set  $Re = 0$ , and the Weissenberg number,  $We = \lambda \bar{u}/b$ , and the viscosity ratio,  $\beta = \mu_s/(\mu_s + \mu_p)$ , characterize channel flows of Oldroyd-B fluids. The Weissenberg number quantifies the ratio between the elastic and viscous forces and is given by the product of the polymer relaxation time,  $\lambda$ , and the velocity gradient,  $\bar{u}/b$ . The steady solution determines the laminar base flow  $(\bar{\mathbf{u}}, \bar{\boldsymbol{\tau}})$ , with  $\bar{\mathbf{u}} = (U(y), 0, 0)$ , where we have  $U(y) = 1 - y^2$  in pressure-driven Poiseuille flow and  $U(y) = y$  in shear-driven Couette flow, and the nonzero components of the base polymer stress tensor,  $\bar{\boldsymbol{\tau}}$ , are  $\bar{\tau}_{11} = 2We[U'(y)]^2$  and  $\bar{\tau}_{12} = \bar{\tau}_{21} = U'(y)$ . Equations for infinitesimal velocity, pressure, and stress fluctuations are obtained by linearization around  $(\bar{\mathbf{u}}, \bar{\boldsymbol{\tau}})$ .

Hoda et al. (2008, 2009) were the first to investigate nonmodal amplification of disturbances in channel flows of viscoelastic fluids and demonstrate high sensitivity of the laminar flow in both inertia- and elasticity-dominated regimes. Jovanović & Kumar (2010) showed that velocity and stress fluctuations experience significant transient growth even in the absence of inertia. Jovanović & Kumar (2011) identified a new slow-fast decomposition of the governing equations and used singular-perturbation techniques to analytically establish unfavorable scaling of the energy amplification with the Weissenberg number in weakly inertial flows. Lieu et al. (2013) quantified

### Dimensionless Oldroyd-B model:

in channel flows of Oldroyd-B fluids (with density  $\rho$  and solvent and polymer viscosities  $\mu_s$  and  $\mu_p$ ), equations can be brought to a nondimensional form by scaling length with the channel half-height,  $b$ ; velocity with the largest velocity of the base flow,  $\bar{u}$ ; time with the polymer relaxation time,  $\lambda$ ; polymer stresses with  $\mu_p \bar{u}/b$ , pressure with  $(\mu_s + \mu_p) \bar{u}/b$ , and forcing per unit mass with  $(\mu_s + \mu_p) \bar{u}/\rho b^2$

the role of finite extensibility of polymers on the worst-case amplification of disturbances in FENE-type models, and Hariharan et al. (2018) studied amplification of localized body forces. The combined effects of inertia and elasticity on streak evolution was examined by Agarwal et al. (2014) and Page & Zaki (2014).

For streamwise-constant flows of Oldroyd-B fluids, the block diagram in **Figure 6b** reflects the structure of the frequency response operator that maps disturbances to the momentum equation (inputs) to the velocity fluctuations (outputs) and eliminates all unnecessary variables. Apart from the operator  $A_{cp2} := ik_z[U'(y)\Delta + 2U''(y)\partial_y]$ , which accounts for stretching of polymer stress fluctuations by a base shear, all other operators are the same as in Newtonian fluids (see Section 3.1.1). The block diagrams reveal striking structural similarity between streamwise-constant inertial flows of Newtonian fluids and inertialess flows of viscoelastic fluids. In the absence of base shear,  $U'(y)$ , and spanwise variations in fluctuations, the responses of viscoelastic fluids are governed by viscous dissipation and all velocity components are  $We$ -independent. However, in contrast to Newtonian fluids, spanwise variations in fluctuations and their interactions with  $U'(y)$  provide a source in the vorticity equation even in the absence of inertia. In particular, the influence of  $d_2$  and  $d_3$  on  $u$  can be understood by analyzing the wall-normal vorticity equation in the dimensionless Oldroyd-B model (Jovanović & Kumar 2011):

$$\beta \Delta \hat{\eta}(t) = -\Delta \eta(t) - (1 - \beta) We [U'(y)\Delta + 2U''(y)\partial_y] ik_z \vartheta(t),$$

where  $\hat{\vartheta} := \hat{v}/(i\omega + 1)$  denotes a low-pass version of the wall-normal velocity,  $v$ . The source term arises from stretching of polymer stress fluctuations by a base shear and it introduces a lift-up of fluctuations in a way similar to vortex tilting in inertia-dominated flows of Newtonian fluids. Thus, the wall-normal and spanwise inputs give rise to an energy transfer from the base flow to fluctuations and generate streamwise velocity fluctuations that are proportional to the Weissenberg number. Responses from all other inputs to all other velocities are  $We$ -independent and are governed by viscous dissipation. Jovanović & Kumar (2011) also demonstrated that  $d_2$  and  $d_3$  induce a quadratic scaling with the Weissenberg number of the streamwise component of the polymer stress tensor,  $\tau_{11}$ .

In summary, elementary control-theoretic analysis identifies key physical mechanisms and demonstrates that the wall-normal and spanwise body forces have the largest impact on the streamwise velocity fluctuations in inertia-dominated channel flows of Newtonian fluids and elasticity-dominated flows of viscoelastic fluids. These conclusions are derived without any computations by examining the frequency responses of streamwise-constant fluctuations and showing that  $d_2$  and  $d_3$  induce a quadratic scaling of  $u$  with the Reynolds number (in Newtonian fluids) and a linear scaling of  $u$  with the Weissenberg number (in inertialess Oldroyd-B fluids). At  $k_x = 0$ ,  $d_1$  does not influence  $v$  and  $w$  and the mappings from all other forcing to all other velocity components are proportional to the Reynolds number (in Newtonian fluids) and are  $We$ -independent (in viscoelastic fluids); readers are referred to Jovanović & Bamieh (2005, section 4) and Jovanović & Kumar (2011) for additional details. Despite these structural similarities, amplification in Newtonian and viscoelastic fluids originates from different physical mechanisms: vortex tilting and polymer stretching, respectively.

### 3.3. Turbulent Channel and Pipe Flows of Newtonian Fluids

Lee et al. (1990) used direct numerical simulations (DNS) of homogeneous turbulence to demonstrate that the linear amplification of eddies that interact with large mean shear induces streamwise streaks even in the absence of a solid boundary. This study also employed linear rapid distortion

theory (Pope 2000) to predict the lack of isotropy and the structure of turbulence at high shear rate. Furthermore, Kim & Lim (2000) used DNS of a turbulent channel flow to show decay of near-wall turbulence in the absence of the linear vortex tilting term.

In contrast to the laminar base flow, the time-averaged turbulent mean velocity is not a solution of the NS equations, and even the question of what to linearize around can be contentious (Beneddine et al. 2016). Since the linearized NS equations around the turbulent mean flow are stable (Malkus 1956, Reynolds & Tiederman 1967), they are well suited for input–output analysis. Butler & Farrell (1993) utilized transient growth analysis over a horizon determined by the eddy turnover time to show that the streak spacing of approximately 100 wall units represents the optimal response of the NS equations linearized around the turbulent mean flow. McKeon & Sharma (2010) employed a gain-based decomposition of fluctuations around mean velocity in turbulent pipe flow to characterize energetic structures in terms of their convection speeds and wavelengths. This study highlighted the role of critical layers in wall-normal localization of experimentally identified energetic modes and related the wave speed,  $c := \omega/k_x$ , to the wall-normal localization of the dominant flow structures. Moarref et al. (2013) leveraged the role of wave speed to formally determine three different scalings for the most amplified modes; showed that these scales are consistent with inner, logarithmic, and outer layers in the turbulent mean velocity; and established dependence of the dominant resolvent modes on the spatial coordinates.

Other classes of linearized models have also been utilized to identify the spatiotemporal structure of the most energetic fluctuations in turbulent flows. In particular, the turbulent mean flow can be obtained as the steady-state solution of the NS equations in which molecular viscosity is augmented with turbulent eddy viscosity (Reynolds & Tiederman 1967, Reynolds & Hussain 1972). Del Álamo & Jiménez (2006), Cossu et al. (2009), Pujals et al. (2009), and Hwang & Cossu (2010a,b) demonstrated that transient growth and input–output analyses of the resulting linearization qualitatively capture features of turbulent flows.

For a turbulent channel flow with  $Re = 547$  and  $k_x = 0$ , **Figure 7** demonstrates the emergence of channel-wide and near-wall streaks in a stochastically forced eddy viscosity–enhanced linearized model. The values of  $k_z$  where the two peaks in the premultiplied energy spectrum,  $k_z E_{k_z}$ , emerge determine the spanwise length scales of the most energetic response of velocity fluctuations to stochastic forcing (**Figure 7a**). Streamwise velocity fluctuations that contain the most variance are harmonic in  $z$ , and their wall-normal shapes are determined by the principal eigenfunctions

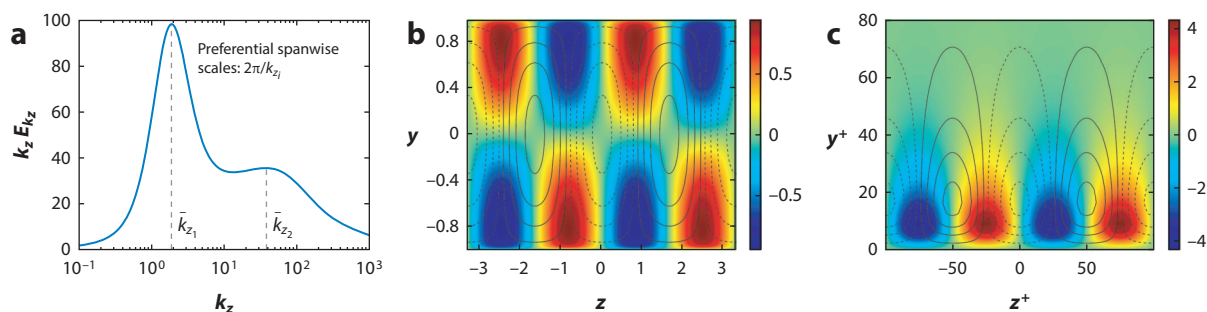


**Figure 7**

(a) Premultiplied energy spectrum,  $k_z E_{k_z}$ , and (b,c) dominant flow structures resulting from stochastically forced eddy viscosity–enhanced linearization around the turbulent mean flow with  $Re = 547$  (based on friction velocity) and  $k_x = 0$ . Color plots display the most energetic streamwise velocity fluctuations,  $u(z, y)$ , and contour lines show streamfunction fluctuations with the spanwise wavelength determined by (b)  $2\pi/\bar{k}_{z1}$  (channel-wide streaks) and (c)  $2\pi/\bar{k}_{z2}$  (near-wall streaks).

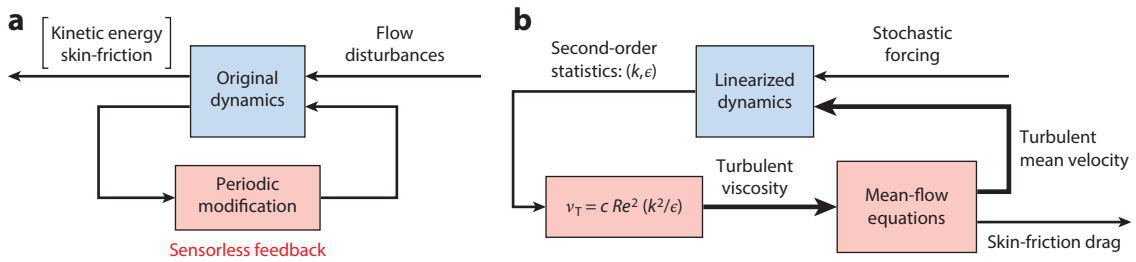


**Figure 8**

Block diagrams of (a) a modification to the dynamics introduced by spatiotemporal oscillations, which introduce a sensorless feedback, at the level of flow fluctuations, by changing a base flow  $U_0(y)$  to a periodic profile, and (b) a simulation-free approach for determining the influence of control on skin-friction drag in turbulent flows. The bold arrows represent coefficients into the mean-flow and linearized equations. In Moarref & Jovanović (2012), the turbulent mean velocity is updated once.

of the stationary covariance operator,  $V_k$  (Figure 7a,b). Pairs of counter-rotating streamwise vortices distribute momentum in the  $(y, z)$ -plane and promote amplification of high- and low-speed streamwise streaks. The most energetic flow structures occupy the entire channel width, and the second set of strongly amplified fluctuations is determined by near-wall streaks.

#### 4. CONTROL OF TRANSITIONAL AND TURBULENT FLOWS

Flow control by sensorless means is often inspired by the desire to bring the efficiency of birds and fish to engineering systems. Control of conductive fluids using the Lorentz force, periodic blowing and suction, wall oscillations, and geometry modifications (e.g., riblets, superhydrophobic surfaces, and jet-engine chevrons) are characterized by the absence of sensing capabilities and implementation of control without measurement of the relevant flow quantities or disturbances. Rather, as illustrated in Figure 8a, the dynamics are impacted by spatiotemporal oscillations through geometry or base velocity modifications.

Min et al. (2006) used DNS to show that a blowing and suction in the form of an upstream traveling wave can provide a sustained sublaminar drag in a fully developed turbulent channel flow. Their paper inspired other researchers to examine fundamental limitations of streamwise traveling waves for control of transitional and turbulent flows (Marusic et al. 2007, Bewley 2009, Fukagata et al. 2009, Höpfner & Fukagata 2009, Lieu et al. 2010, Moarref & Jovanović 2010). Furthermore, simulations and experiments showed that spanwise wall oscillations can reduce skin-friction drag by as much as 45% (Jung et al. 1992, Laadhari et al. 1994, Choi et al. 1998, Choi 2002, Ricco 2004). While these and other studies (e.g., Fransson et al. 2006) have demonstrated the potential of sensorless periodic strategies, until recently a model-based design for transitional and turbulent flows remained elusive.

In Section 4.1, we highlight the utility of the input–output framework in the design of traveling waves for controlling the onset of turbulence while achieving positive net efficiency (Moarref & Jovanović 2010), and in Section 4.2, we describe how stochastic analysis in conjunction with control-oriented turbulence modeling quantifies the effect of control on turbulent flow dynamics and identifies the optimal period of oscillations for drag reduction (Moarref & Jovanović 2012). Apart from demonstrating the merits of the input–output approach in the design of periodic strategies for controlling laminar and turbulent flows, we also illustrate how to overcome challenges that arise in secondary receptivity analysis, i.e., in nonmodal analysis of the dynamics associated with spatially or time-periodic base flows.

## 4.1. Controlling the Onset of Turbulence by Streamwise Traveling Waves

Let channel flow be subject to a uniform pressure gradient and a zero-net mass-flux blowing and suction along the walls,  $V(y = \pm 1) = \mp 2\alpha \cos(\omega_x(\bar{x} - ct))$  (see **Figure 1b**). Here,  $\alpha$ ,  $\omega_x$ , and  $c$  respectively denote amplitude, frequency, and speed of the wave that travels in the streamwise direction,  $\bar{x}$ . Positive/negative values of  $c$  identify downstream/upstream waves, and  $c = 0$  gives a standing wave. The Galilean transformation,  $x := \bar{x} - ct$ , eliminates the time dependence in  $V(\pm 1)$ , and the steady-state solution of the NS equations,  $\bar{\mathbf{u}} = (U(x, y), V(x, y), 0)$ , does not depend on  $t$  in the frame of reference that travels with the wave. The new laminar base flow,  $\bar{\mathbf{u}}$ , is no longer a parabola: It is periodic in  $x$ , with frequency  $\omega_x$ , and it contains both streamwise and wall-normal components,  $U(x, y)$  and  $V(x, y)$ .

**4.1.1. Net efficiency of modified base flow.** Blowing and suction induce a bulk flux in the direction opposite to that of the wave (Hoepffner & Fukagata 2009). This pumping mechanism occurs even in the absence of the pressure gradient and is explained by a weakly nonlinear analysis. For small-amplitude  $\alpha$ ,  $U(x, y)$  is given by

$$U(x, y) = \begin{array}{lll} \text{Parabola} & \text{Mean drift} & \text{Oscillatory components} \\ U_0(y) & + \alpha^2 U_{20}(y) & + \alpha [U_{1p}(y) e^{i\omega_x x} + U_{1m}(y) e^{-i\omega_x x}] \\ & & + \alpha^2 [U_{2p}(y) e^{i2\omega_x x} + U_{2m}(y) e^{-i2\omega_x x}] + \mathcal{O}(\alpha^3). \end{array}$$

In addition to an oscillatory  $\mathcal{O}(\alpha)$  correction to  $U_0(y)$  with frequency  $\omega_x$ , both the second harmonic  $2\omega_x$  and the mean flow correction  $U_{20}(y)$  are induced by the quadratic nonlinearity in the NS equations at the level of  $\alpha^2$ . For the fixed pressure gradient, the skin-friction drag coefficient of the base flow is inversely proportional to the square of the bulk flux. Since the integral of  $U_{20}(y)$  is positive for the upstream and negative for the downstream waves (Hoepffner & Fukagata 2009, Moarref & Jovanović 2010), upstream/downstream waves respectively reduce/increase skin-friction drag coefficient relative to the laminar uncontrolled flow.

The net efficiency of wall actuation is given by the difference of the produced and required powers (Quadrio & Ricco 2004). These two quantities respectively determine the increase/decrease in bulk flux relative to the flow with no control and the control effort exerted at the walls. Compared to laminar uncontrolled flow, any strategy based on blowing and suction reduces net efficiency (Bewley 2009, Fukagata et al. 2009). However, if uncontrolled flow becomes turbulent, both upstream and downstream waves of small enough amplitudes can improve net efficiency (Moarref & Jovanović 2010, section 2.4). Moarref & Jovanović (2010) also demonstrated that, apart from the net efficiency, the dynamics of fluctuations around the modified base flow have to be evaluated when designing the traveling waves.

**4.1.2. Dynamics of velocity fluctuations.** The laminar base flow induced by the traveling waves is periodic in  $x$ , with frequency  $\omega_x$ , and the resulting linearization is not translationally invariant in the streamwise direction. The normal modes in  $z$  are still harmonic,  $e^{ik_z z}$ , but in  $x$  they are given by the Bloch waves, which are determined by a product of  $e^{i\theta x}$  and the  $2\pi/\omega_x$ -periodic function in  $x$ ,  $\tilde{\mathbf{d}}_{\mathbf{k}}(x, y, t) = \tilde{\mathbf{d}}_{\mathbf{k}}(x + 2\pi/\omega_x, y, t)$ :

$$\mathbf{d}(x, y, z, t) = \tilde{\mathbf{d}}_{\mathbf{k}}(x, y, t) e^{i(\theta x + k_z z)} = \sum_{n=-\infty}^{\infty} \tilde{\mathbf{d}}_{\mathbf{k},n}(y, t) e^{i[(\theta + n\omega_x)x + k_z z]}, \quad \theta \in [0, \omega_x),$$

where  $\mathbf{k} := (\theta, k_z)$  and  $\tilde{\mathbf{d}}_{\mathbf{k},n}(y, t)$  are the coefficients in the Fourier series expansions of  $\tilde{\mathbf{d}}_{\mathbf{k}}(x, y, t)$ . In this case, signals in Equation 1 are the  $\mathbf{k}$ -parameterized bi-infinite column vectors whose components are determined by the corresponding Fourier series coefficients, e.g.,

$\mathbf{d}_k(t) := \text{col}\{\tilde{\mathbf{d}}_{k,n}(y, t)\}_{n \in \mathbb{Z}}$ , and similarly for  $\psi_k(t)$  and  $\xi_k(t)$ . Thus, for each  $\mathbf{k}$ ,  $A_k$ ,  $B_k$ , and  $C_k$  in Equation 1 are bi-infinite matrices whose entries are operators in the wall-normal direction,  $y$  (Moarref & Jovanović 2010), and the frequency response operator  $T_k(i\omega)$  defined in the sidebar titled Frequency Response Operator maps  $\hat{\mathbf{d}}_k(i\omega) := \text{col}\{\hat{\mathbf{d}}_{k,n}(y, i\omega)\}_{n \in \mathbb{Z}}$  to  $\hat{\xi}_k(i\omega) := \text{col}\{\hat{\xi}_{k,n}(y, i\omega)\}_{n \in \mathbb{Z}}$ .

Since modal stability does not capture the early stages of transition, Moarref & Jovanović (2010) utilized input–output analysis of a linearization around  $(U(x, y), V(x, y), 0)$  to quantify the effect of control on amplification of stochastic disturbances and identify waves that reduce receptivity relative to the flow without control. A discretization in  $y$  and truncation of bi-infinite matrices in Equation 1 yield a large-scale Lyapunov Equation 7; computing its solution to assess impact of control parameters  $(\alpha, \omega_x, c)$ , wave numbers  $(\theta, k_z)$ , and the Reynolds number  $Re$  on the energy amplification is demanding. Motivated by the observation that large values of  $\alpha$  introduce high cost of control, Moarref & Jovanović (2010) employed a perturbation analysis to efficiently compute the solution to Equation 7. This approach offers significant advantages relative to the approach based on truncation: The impact of small-amplitude waves on energy amplification can be assessed via computations that are of the same complexity as computations in the uncontrolled flow. In particular, for small-amplitude waves, the following explicit formula,

$$\frac{\text{energy amplification with control}}{\text{energy amplification without control}} = 1 + \alpha^2 g_k(\omega_x, c, Re) + \mathcal{O}(\alpha^4), \quad 13.$$

offers insights into the impact of control on energy amplification. For  $\alpha \ll 1$ , the analysis amounts to examining the dependence of the function  $g_k$  in Equation 13 on  $\mathbf{k} = (\theta, k_z)$ ; the frequency/speed of the wave,  $(\omega_x, c)$ ; and the Reynolds number,  $Re$ . Positive (negative) values of  $g_k$  respectively identify parameters that increase (decrease) energy amplification. For channel flow with  $Re = 2,000$  and fixed values of  $\omega_x$  and  $c$ , we use a sign-preserving logarithmic scale to visualize the  $\mathbf{k}$ -dependence of the function  $g_k$  in **Figure 9**. While the downstream waves with  $(\omega_x = 2, c = 5)$  reduce amplification for all values of  $\theta$  and  $k_z$ , the upstream waves with  $(\omega_x = 0.5, c = -2)$  promote amplification for a broad range of  $\theta$  and  $k_z$ . Thus, in addition to guaranteeing positive

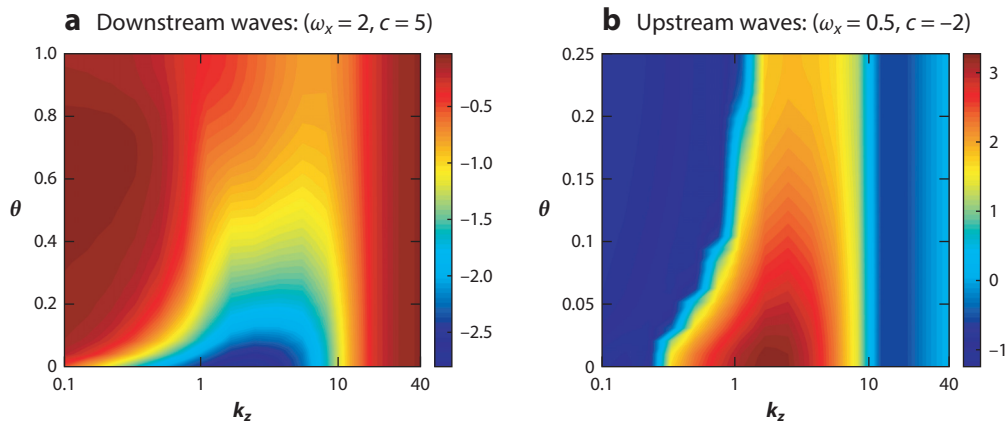


**Figure 9**

The second-order correction to the energy amplification in Equation 13 visualized using a sign-preserving logarithmic scale,  $\text{sign}(g_k)\log_{10}(1 + |g_k|)$ , in channel flow with  $Re = 2,000$  (based on the centerline velocity of the parabolic laminar profile and the channel half-height). While the downstream waves with selected parameters reduce amplification for all values of  $\theta$  and  $k_z$ , the upstream waves promote amplification for a broad range of  $\theta$  and  $k_z$ . Figure adapted with permission from Moarref & Jovanović (2010), copyright 2010 Cambridge University Press.



net efficiency relative to the uncontrolled flow that becomes turbulent (see Section 4.1.1), the downstream waves also suppress energy of 3D fluctuations. In contrast, the upstream waves with the parameters that provide a favorable skin-friction coefficient of the modified laminar flow (Min et al. 2006) increase amplification of the most energetic modes of the uncontrolled flow. In fact, since, at best, they exhibit receptivity similar to that of the uncontrolled flow (Moarref & Jovanović 2010) and can even induce modal instability of the modified laminar flow (Lee et al. 2008), they are not suitable for controlling the onset of turbulence. In contrast, properly designed downstream waves can substantially reduce the production of fluctuations' kinetic energy (Moarref & Jovanović 2010) and are an excellent candidate for preventing transition to turbulence.

**4.1.3. Verification by direct numerical simulation.** All theoretical predictions resulting from the simulation-free approach of Moarref & Jovanović (2010) were verified by Lieu et al. (2010). Their DNS confirmed that the downstream waves indeed provide an effective means for controlling the onset of turbulence and that the upstream waves promote transition even when the uncontrolled flow stays laminar. This demonstrates considerable predictive power of the input–output framework and suggests that reducing receptivity is a viable approach to controlling transition.

## 4.2. Turbulent Drag Reduction by Spanwise Wall Oscillations

Spanwise wall oscillations can reduce turbulent drag by as much as 45%. This observation was made in simulations, experiments, and theoretical studies (Dhanak & Si 1999, Bandyopadhyay 2006, Ricco & Quadrio 2008) that focused on explaining the effectiveness of this sensorless strategy. Here we describe how input–output analysis in conjunction with control-oriented turbulence modeling identifies the optimal period of oscillations for turbulence suppression in channel flow (see Moarref & Jovanović 2012 for details).

**4.2.1. Modified mean flow.** In pressure-driven channel flow, the steady-state solution of the NS equations in which the molecular viscosity is augmented with the turbulent viscosity  $\nu_{T0}(y)$  is determined by the Reynolds–Tiederman profile,  $U_0(y)$ . If the flow is also subject to  $W(y = \pm 1, t) = 2\alpha \sin(\omega t)$ , the steady-state solution is given by  $(U_0(y), 0, W_0(y, t)) = \alpha[W_p(y)e^{i\omega t} + W_p^*(y)e^{-i\omega t}]$ . Here,  $U_0(y)$  approximates the mean streamwise velocity of the uncontrolled turbulent flow and the wall oscillations induce the time-periodic spanwise component,  $W_0(y, t)$ , under the assumption that the turbulent viscosity is not modified by control. If this were the case, the oscillations would have no impact on  $U_0$ , which is at odds with simulations/experiments. In contrast, the estimates of the required power exerted by wall oscillations resulting from the use of  $W_0$  closely match the DNS results of Quadrio & Ricco (2004) over a broad range of oscillation periods (Moarref & Jovanović 2012, section 2.2).

**4.2.2. Turbulence modeling.** The inability of the above approach to predict drag reduction arises from the fact that the wall oscillations change the turbulent viscosity of the flow with no control. Moarref & Jovanović (2012) pioneered a method based on the stochastically forced eddy viscosity-enhanced NS equations linearized around  $(U_0(y), 0, W_0(y, t))$  to capture the influence of control on turbulent viscosity. The approach utilizes the Boussinesq hypothesis, but in contrast to standard practice, the turbulent kinetic energy,  $k$ , and its rate of dissipation,  $\epsilon$ , are computed using the second-order statistics of velocity fluctuations in the linearized model. Using an analogy with homogeneous isotropic turbulence, Moarref & Jovanović (2012, section 3.1) selected spatial correlations of white-in-time forcing to provide equivalence between the 2D energy spectra of the uncontrolled turbulent flow and the flow governed by the stochastically forced linearization

around  $(U_0(y), 0, 0)$ . This approach was the first to utilize available DNS data (del Álamo & Jiménez 2003, del Álamo et al. 2004) of the uncontrolled turbulent flow to guide control-oriented modeling for design purposes; it takes advantage of the turbulent viscosity and the energy spectrum of the uncontrolled flow and determines the effect of control on the turbulent flow using a model-based approach.

**4.2.3. Dynamics of velocity fluctuations.** Linearization around  $(U_0(y), 0, W_0(y, t))$  yields a time-periodic model with  $A_{\mathbf{k}}(t) = A_{\mathbf{k},0} + \alpha (A_{\mathbf{k},-1}e^{-i\omega_y t} + A_{\mathbf{k},1}e^{i\omega_y t})$ , and the solution to Equation 11 provides two-point correlations. For small-amplitude oscillations, Moarref & Jovanović (2012) utilized perturbation analysis to efficiently solve this equation and identify the oscillation periods that yield the largest drag reduction and net efficiency. This approach quantifies the influence of velocity fluctuations on the turbulent viscosity in the flow with control,  $\nu_T(y) = \nu_{T0}(y) + \alpha^2 \nu_{T2}(y) + \mathcal{O}(\alpha^4)$ , where  $\nu_{T0}(y)$  is the turbulent viscosity of the uncontrolled flow and  $\nu_{T2}(y)$  is determined by the second-order corrections (in  $\alpha$ ) to the kinetic energy,  $k_2(y)$ , and its rate of dissipation,  $\epsilon_2(y)$ . These quantities are obtained by averaging the second-order statistics resulting from a stochastically forced linearization around  $(U_0(y), 0, W_0(y, t))$  over the wall-parallel directions and one period of oscillations.

The solution to Equation 11 and the above expression for  $\nu_T$  are used to assess the influence of small-amplitude oscillations on the dynamics of velocity fluctuations and to identify the optimal period of oscillations for drag reduction. For the controlled flow with constant bulk flux and the friction Reynolds number  $Re = 186$ , **Figure 10** shows the second-order correction to the skin-friction coefficient  $\%C_{f2}(T^+)$ , normalized by its largest value, and normalized DNS results at  $Re = 200$  (Quadrio & Ricco 2004). A close agreement is observed between a theoretical prediction for the optimal period resulting from input–output analysis ( $T^+ = 102.5$ ) and DNS results ( $T^+ \approx 100$ ). **Figure 10b,c** shows the premultiplied 2D energy spectrum of the uncontrolled flow,  $k_x k_z E_{\mathbf{k},0}$ , and the second-order correction,  $k_x k_z E_{\mathbf{k},2}$ , triggered by small-amplitude oscillations with the optimal period  $T^+ = 102.5$ . The most energetic modes of the uncontrolled flow occur at  $(k_x \approx 2.5, k_z \approx 6.5)$ . **Figure 10c** shows that the wall oscillations increase amplification of the modes with small streamwise wavelengths, in addition to suppression of energy of large streamwise

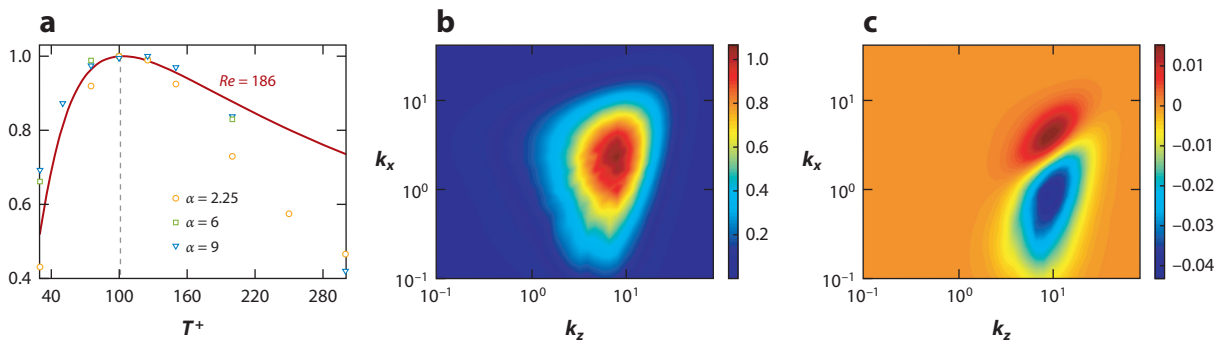


**Figure 10**

(a) Second-order correction (in  $\alpha$ ) to the skin-friction drag coefficient relative to the uncontrolled flow,  $\%C_{f2}(T^+)$ , normalized by  $\max_{T^+} \%C_{f2}(T^+)$ , as a function of the period of oscillations,  $T^+$ , for the flow with  $Re = 186$  and DNS (direct numerical simulation)-based  $\%C_{f2}(T^+)$  normalized by the corresponding largest values at  $Re = 200$  (Quadrio & Ricco 2004) for control amplitudes  $\alpha = 2.25$ ,  $\alpha = 6$ , and  $\alpha = 9$ . (b) Premultiplied DNS-based energy spectrum,  $k_x k_z E_{\mathbf{k},0}$ , of the uncontrolled turbulent flow with  $Re = 186$ . (c) Second-order correction to the energy spectrum,  $k_x k_z E_{\mathbf{k},2}$ , for the flow subject to wall oscillations with optimal drag-reducing period  $T^+ = 102.5$ . Figure adapted with permission from Moarref & Jovanović (2012), copyright 2012 Cambridge University Press.

wavelengths. This observation agrees with the study of the impact of wall oscillations on free-stream vortices in a pretransitional boundary layer (Ricco 2011). Moarref & Jovanović (2012) also showed that the optimal wall oscillations minimize the turbulent viscosity near the interface of the buffer and log-law layers and that oscillations are less effective at higher Reynolds numbers.

**4.2.4. Summary.** Traveling waves and wall oscillations introduce a sensorless feedback via periodic modifications to the dynamics (see **Figure 8a**) by changing a base flow  $U_0(y)$  to a spatially or time-periodic profile. Depending on the actuation waveform and the parameters, the properties can be improved or worsened relative to the flow without control. In contrast to a standard approach, which employs DNS and experiments to assess sensorless periodic strategies, Moarref & Jovanović (2010, 2012) developed a model-based framework for determining the influence of control on transitional and turbulent flows and demonstrated the critical importance of the dynamics associated with the modified base flows for effectively controlling the onset of turbulence and drag reduction. The developed simulation-free method enables computationally efficient design by merging receptivity analysis and control-oriented turbulence modeling with techniques from control theory, and its utility goes beyond the case studies presented here. Recently, the input–output approach was used to quantify the effect of riblets on kinetic energy and turbulent drag in channel flow (Chavarin & Luhar 2020, Ran et al. 2020) and it is expected to enable optimal design of periodic strategies for control of transitional and turbulent flows. The input–output framework is also at the heart of the optimal and robust  $H_2$  and  $H_\infty$  feedback control strategies (Zhou et al. 1996) and has recently found use in the model-based design of opposition control (Luhar et al. 2014, Toedtli et al. 2019).

## 5. PHYSICS-AWARE DATA-DRIVEN TURBULENCE MODELING

Advances in high-performance computing and measurement techniques provide an abundance of data for a broad range of flows. Thus, turbulence modeling can be formulated as an inverse problem, where the objective is to identify a parsimonious model that explains available data and generalizes to unavailable data. Techniques from machine learning and statistical inference were recently employed to reduce uncertainty and improve the predictive power of models based on the Reynolds-averaged NS equations (Duraisamy et al. 2019). Large data sets can also be exploited to develop reduced dynamical representations (Rowley & Dawson 2017), but an exclusive reliance on data makes such models agnostic to physical constraints and can yield subpar performance in regimes that are not contained in the training data set. Moreover, sensing and actuation can significantly change the identified model, thereby making its use for flow control challenging (Noack et al. 2011, Tadmor & Noack 2011). A compelling alternative for model-based optimization and control is to leverage data in conjunction with a prior model that arises from first principles.

As demonstrated in Section 3, the linearized NS equations in the presence of stochastic excitation can be used to qualitatively predict structural features of transitional and turbulent shear flows. In most prior studies, excitations were restricted to white-in-time stochastic inputs but this assumption is often too narrow to fully capture observed statistics of turbulent flows (Jovanović & Georgiou 2010). To overcome these limitations, Zare et al. (2017a,b) developed a framework to allow for colored-in-time inputs to the linearized NS equations.

We next briefly summarize how strategic use of data enhances the predictive power of the linearized NS equations in order to capture second-order statistics of turbulent flows (Zare et al. 2017a,b, 2020a). Since machine learning tools are physics agnostic, the power spectrum of stochastic forcing is identified by merging tools from control theory and convex optimization. The resulting stochastic model, given by Equation 10, accounts for neglected nonlinear interactions via a low-rank perturbation to the original dynamics (see **Figure 11**).

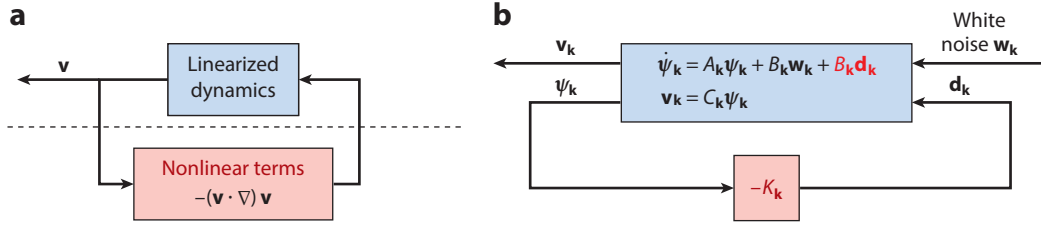


**Figure 11**

(a) The Navier–Stokes (NS) equations can be viewed as a feedback interconnection of the linearized dynamics with the nonlinear term. (b) Stochastically driven linearized NS equations with low-rank state feedback modification. At the level of second-order statistics, the two representations can be made equivalent by proper selection of  $B_k$  and  $K_k$  (cf. Equation 10).

### 5.1. Completion of Partially Available Channel Flow Statistics

Here we examine linearization around mean velocity in turbulent channel flow and highlight the utility of the framework developed in Zare et al. (2017a,b). A pseudo-spectral method (Weideman & Reddy 2000) yields a finite-dimensional approximation of the operators in  $y$ , and a change of variables (Zare et al. 2017b, appendix A) leads to an evolution model in which the kinetic energy at any  $\mathbf{k}$  is determined by the Euclidean norm of the state vector  $\psi_k$ . For given  $(A_k, B_k)$  and input statistics  $(W_k$  or  $H_k)$ , algebraic Equations 7 and 8 can be used to compute the stationary covariance matrix  $X_k$  of the state  $\psi_k$  in the system described by Equation 1. However, in turbulence modeling, the converse question arises: Starting from Equation 1 and the covariance matrix  $X_k$  (resulting from DNS or experiments), can we identify the power spectrum of the stochastic input  $\mathbf{d}_k(t)$  that generates such statistics? For the NS equations linearized around turbulent mean velocity with white-in-time stochastic forcing, the answer to this question is negative (Zare et al. 2017b, figure 6). This limitation can be overcome by allowing for colored-in-time stochastic inputs to the linearized system described by Equation 1.

The positive-definite matrix  $X_k$  is the stationary covariance of the state  $\psi_k(t)$  of the LTI system described by Equation 1 with controllable pair  $(A_k, B_k)$  if and only if (Georgiou 2002a,b) the following holds:

$$\text{rank} \begin{bmatrix} A_k X_k + X_k A_k^* & B_k \\ B_k^* & 0 \end{bmatrix} = \text{rank} \begin{bmatrix} 0 & B_k \\ B_k^* & 0 \end{bmatrix}. \quad 14.$$

This fundamental condition guarantees that, for given  $A_k, B_k$ , and  $X_k$ , Equation 8 can be solved for  $H_k$ . It also implies that any  $X_k = X_k^* > 0$  is admissible as a stationary covariance of  $\psi_k(t)$  in Equation 1 if the input matrix  $B_k$  is full rank. In particular, for  $B_k = I$ , Equation 8 is satisfied with  $H_k^* = -A_k X_k$ , and the stochastically forced system described by Equation 10, which simplifies to  $\dot{\psi}_k(t) = -(1/2)X_k^{-1}\psi_k(t) + \mathbf{w}_k(t)$  for this choice of  $H_k$  and  $W_k = I$ , can be used to generate  $X_k$ . This implies that a colored-in-time input that excites all degrees of freedom in Equation 1 can completely cancel the relevant physics contained in  $A_k$ . Thus, in data-driven turbulence modeling, it is critically important to restrict the rank of the matrix  $B_k$ , which specifies the number of inputs to the linearized NS equations.

To address this challenge, Zare et al. (2017a,b) formulated and solved the problem of completing a subset of entries  $V_{k,ij}^{\text{dns}}$  of the stationary covariance matrix  $V_k^{\text{dns}}$  of velocity fluctuations using stochastically forced linearization around the turbulent mean velocity. The approach utilizes algebraic Equation 8 with  $Z_k := B_k H_k^* + H_k B_k^*$  and a maximum entropy formalism along with a convex surrogate for rank minimization to limit the number of inputs to the linearized model and

identify spectral content of the colored-in-time forcing:

$$\begin{aligned}
 & \underset{X_k, Z_k}{\text{minimize}} \quad -\log \det(X_k) + \gamma \sum_i \sigma_i(Z_k), & \text{Objective function} \\
 & \text{subject to} \quad A_k X_k + X_k A_k^* + Z_k = 0, & \text{Physics} \\
 & \quad (C_k X_k C_k^*)_{ij} = V_{k,ij}^{\text{dns}}, \quad (i, j) \in \mathcal{I}. & \text{Available data}
 \end{aligned} \tag{15}$$

The Hermitian matrices  $X_k \succ 0$  and  $Z_k$  are the optimization variables, whereas the matrices  $(A_k, C_k)$ , the available entries  $V_{k,ij}^{\text{dns}}$  of  $V_k^{\text{dns}}$  for a selection of indices  $(i, j) \in \mathcal{I}$ , and  $\gamma > 0$  are known problem parameters. The first constraint in Equation 15 comes from physics; it imposes the requirement that second-order statistics are consistent with linearization around turbulent mean velocity. The second constraint requires that the available elements of the matrix  $V_k^{\text{dns}}$  are exactly reproduced by the linearized model. The logarithmic barrier function is introduced to ensure positive-definiteness of  $X_k$  (Boyd & Vandenberghe 2004), and the sum of singular values of the matrix  $Z_k$ , which reflects the contribution of the stochastic input, is used as a convex proxy to restrict the rank of  $Z_k$  (Fazel 2002, Recht et al. 2010).

The convexity of the objective function and the linearity of the constraint set in Equation 15 imply the existence of a unique globally optimal solution,  $(X_k^*, Z_k^*)$ . This solution reproduces all available entries of the stationary covariance matrix  $V_k^{\text{dns}}$  resulting from DNS (or experiments) and completes unavailable second-order statistics via the low-complexity stochastic dynamical model given by Equation 10. In particular, the factorization of  $Z_k^*$  can be used to determine  $B_k^*$  and  $H_k^*$ , which, along with  $X_k^*$ , yield a low-rank modification,  $B_k^* K_k^*$ , to  $A_k$  in Equation 10. This approach provides a model that refines the predictive power of the linearized NS equations by employing data while preserving the relevant physics of turbulent flows.

**Figure 12** shows the covariance matrices  $V_{k,uu}$  and  $V_{k,uw}$  resulting from DNS of turbulent channel flow with  $Re = 186$  (**Figure 12a,c**) and the solution to the optimization problem in Equation 15 with  $\gamma = 300$  (**Figure 12b,d**) for  $\mathbf{k} = (2.5, 7)$ . The lines along the main diagonals mark the one-point correlations (in  $y$ ) that are used as available data in Equation 15 and are perfectly matched. Using a Frobenius norm measure,  $\|V_k^* - V_k^{\text{dns}}\|_F / \|V_k^{\text{dns}}\|_F$ , approximately 60% of  $V_k^{\text{dns}}$  can be recovered by the stationary covariance matrix,  $V_k^* = C_k X_k^* C_k^*$ , of velocity fluctuations resulting from the solution of Equation 15 (Zare et al. 2017b). The high-quality recovery of two-point correlations is attributed to the Lyapunov-like structural constraint in Equation 15, which keeps physics in the mix and enforces consistency between data and the linearized dynamics.

## 5.2. Alternative Formulations

The covariance completion problem in Equation 15 can be cast as an optimal control problem aimed at establishing a trade-off between control energy and the number of feedback couplings that are required to modify  $A_k$  in the system described by Equation 10 and achieve consistency with available data (Zare et al. 2020a,b). Depending on the modeling purpose and available data, many alternative turbulence modeling formulations are possible. Jovanović & Bamieh (2001) showed that portions of one-point correlations in  $(x, y, z)$ , resulting from the integration of DNS-based  $V_k^{\text{ker}}(y, y)$  over  $\mathbf{k}$ , can be approximated by the appropriate choice of covariance of white-in-time forcing to the NS equations linearized around the turbulent mean velocity. This early success inspired the development of optimization algorithms for the approximation of full covariance matrices using stochastic dynamical models (Høpfner 2005, Lin & Jovanović 2009). For the eddy viscosity-enhanced linearization, Moarref & Jovanović (2012) demonstrated that white-in-time forcing with variance proportional to the turbulent energy spectrum can be used to reproduce the DNS-based energy spectrum of velocity fluctuations. Hwang & Eckhardt (2020) determined the wave number dependence of the variance of stochastic forcing, which is uncorrelated in  $t$  and  $y$ , and minimizes the difference between the Reynolds shear stresses resulting from the mean and the

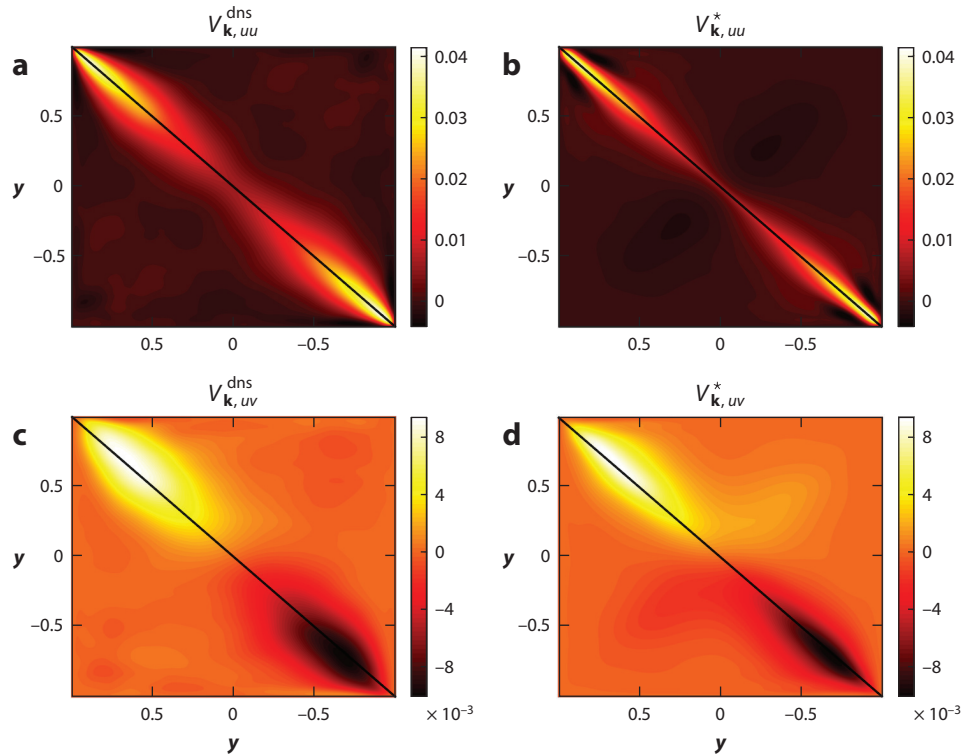


**Figure 12**

(*a,b*) Streamwise,  $V_{\mathbf{k},uu}$ , and (*c,d*) streamwise/wall-normal,  $V_{\mathbf{k},uv}$ , covariance matrices resulting from direct numerical simulation of turbulent channel flow with  $Re = 186$  (*a,c*), and the solution to the optimization problem in Equation 15 with  $\gamma = 300$  (*b,d*) for  $\mathbf{k} = (2.5, 7)$ . Black lines along the main diagonals mark the one-point correlations that are used as available data in Equation 15 and are perfectly matched. Figure adapted with permission from Zare et al. (2017b), copyright 2017 Cambridge University Press.

linearized eddy viscosity-enhanced NS equations. Several recent efforts were aimed at matching individual entries of the spectral density matrix  $S_{\mathbf{k}}(i\omega)$  at given frequencies (Beneddine et al. 2016, 2017; Towne et al. 2020) or at capturing the spectral power,  $\text{trace}(S_{\mathbf{k}}(i\omega))$  (Morra et al. 2019). Finally, compared to the standard resolvent analysis (Moarref et al. 2014), an optimization-based approach that utilizes a componentwise approach (Rosenberg & McKeon 2019) offers considerable improvement in matching spectra and cospectra in turbulent channel flow (McMullen et al. 2020). This further exemplifies the power and versatility of the componentwise input–output viewpoint of fluid flows that was introduced by Jovanović & Bamieh (2005).

## 6. DISCUSSION

In this section we expand on future issues and provide an overview of outstanding challenges.

### 6.1. Complex Fluids and Complex Flows

In addition to parallel flows, input–output analysis was utilized to quantify the influence of deterministic (Sipp & Marquet 2013) and stochastic (Ran et al. 2019b) inputs as well as base flow variations (Brandt et al. 2011) on spatially evolving boundary layers. In high-speed compressible flows, there is a coupling of inertial and thermal effects, and experiments suggest a significant



impact of exogenous disturbances on transition (Fedorov 2011). Traditional receptivity is based on a local spatial analysis (Malik 1989, Bertolotti & Herbert 1991) and is not applicable to most bodies of aerodynamic interest. For hypersonic vehicles with complex geometry or shock interactions with control surfaces, transition is poorly understood, and empirical testing is typically used to characterize their behavior. Linearization around spatially evolving base flows in the presence of sharp gradients involves multiple inhomogeneous directions, and even modal stability analysis becomes challenging and computationally demanding (Hildebrand et al. 2018, Sidharth et al. 2018). Recently, Dwivedi et al. (2019) employed a global input–output analysis to quantify the amplification of exogenous disturbances and explain the appearance of experimentally observed steady reattachment streaks in a hypersonic flow over a compression ramp. For the laminar shock–boundary layer interaction, this study showed that upstream counter-rotating vortices trigger streaks with a preferential spanwise length scale. Input–output analysis is expected to clarify the importance of different physical mechanisms in the presence of surface roughness and free-stream disturbances and to quantify the impact of modeling uncertainties that arise from chemical reactions and gas surface interactions on hypersonic flows (Candler 2019).

## 6.2. Computational Complexity

For an evolution model with  $n$  degrees of freedom, the tools presented in this review require  $\mathcal{O}(n^3)$  computations. Such computations are routine for canonical flows, but the large-scale nature of spatially discretized models in complex geometries induces significant computational overhead. Dominant singular values of the state-transition and frequency response operators can be computed iteratively (Schmid 2007) or via randomized techniques (Halko et al. 2011). Such computations have been used to conduct nonmodal analysis of complex flows (Jeun et al. 2016; Dwivedi et al. 2019, 2020). While in general it is challenging to efficiently solve large-scale Lyapunov equations, efficient iterative algorithms (in terms of both memory and computations) exist for systems with a small number of inputs and outputs and sparse dynamic matrices (Benner et al. 2008). These are expected to bring the utility of stochastic analysis from canonical channels (Jovanović & Bamieh 2005) and boundary layers (Ran et al. 2019b) to flows in complex geometries.

## 6.3. Nonlinear Interactions

Large amplification of disturbances in conjunction with nonlinear interactions can induce secondary instability of streamwise streaks, their breakdown, and transition (Waleffe 1997). An alternative self-sustaining mechanism shows that turbulence can be triggered by the streamwise-constant NS equations in feedback with a stochastically forced streamwise-varying linearization (Farrell & Ioannou 2012, Thomas et al. 2014). Nonlinear nonmodal stability analysis identifies initial conditions of a given amplitude that maximize energy at a fixed time (Kerswell 2018). Dissipation inequalities (Ahmadi et al. 2019) and a harmonic balance approach (Rigas et al. 2020) were recently utilized to extend input–output analysis to the nonlinear NS equations, parabolized Floquet equations were employed to examine the interactions among different modes in slowly varying shear flows (Ran et al. 2019a), and the theory of integral quadratic constraints (Megretski & Rantzer 1997) was used to study a phenomenological model of transition (Kalur et al. 2020). However, it is still an open challenge to precisely characterize the interplay between high flow sensitivity and nonlinearity in order to capture later stages of transition routes and design effective control strategies.

## 6.4. Data-Driven Techniques

Machine learning has revolutionized many disciplines, e.g., image recognition and speech processing, and is increasingly used in modeling and decision making based on available data. While

the NS equations are often too complex for model-based optimization and control, DNS provides data for reduced-order dynamical modeling (Rowley 2005, Lumley 2007, Schmid 2010, Jovanović et al. 2014, Towne et al. 2018). Capitalizing on the availability of such data, machine and reinforcement learning have recently been used for flow modeling, optimization, and control (Brunton et al. 2020) and this trend will continue. In spite of the apparent promise, several challenges have to be addressed, including the development of methods that respect physical constraints, generalize to flow regimes that were not accounted for in the available data sets, and offer convergence, performance, and robustness guarantees on par with model-based approaches to flow control.

## 6.5. Feedback Control

Feedback control offers a more viable approach than sensorless control for dealing with uncertainties that impact the operation of engineering flows. The scale and complexity of the problem introduce significant challenges for modeling, sensor and actuator placement, and control design. These necessitate the development of model-based and data-driven techniques. In wall-bounded flows at low Reynolds numbers, model-based feedback control has shown significant promise (Joshi et al. 1997; Bewley & Liu 1998; Högberg et al. 2003a,b; Kim & Bewley 2007). Since sensing and actuation are typically restricted to the surface, the flow field needs to be estimated using limited noisy measurements in order to form a control action. Hoepffner et al. (2005) and Chevalier et al. (2006) demonstrated the importance of statistics of disturbances in the design of estimation gains. Alternatively, the data-refined model, given by Equation 10, which matches statistics of turbulent flows, can be readily embedded into a Kalman filter estimation framework. Alongside estimation, challenges associated with the optimal sensor and actuator placement (Chen & Rowley 2011, Dhingra et al. 2014, Zare et al. 2020b), efficient computation of optimal and robust controllers (Bewley et al. 2016), structured and distributed control synthesis (Lin et al. 2013), and convergence and sample complexity of data-driven reinforcement learning strategies (Mohammadi et al. 2019) have to be addressed to enable successful feedback control at high Reynolds numbers.

### SUMMARY POINTS

1. The following quote is attributed to Eric Eady: “It is not the process of linearization that limits insight. It is the nature of the state that we choose to linearize about” (Boyd 2001, p. 127). In addition, this review demonstrates that the tools that we use to study the linearized equations are as important as the base flow that we choose to linearize about.
2. Componentwise input–output analysis goes beyond and enhances standard resolvent analysis. In channel flows of Newtonian fluids, it uncovers mechanisms for subcritical transition and identifies streamwise streaks, oblique waves, and Orr–Sommerfeld modes as input–output resonances from forcing to velocity components.
3. Input–output analysis discovers a viscoelastic analog of the familiar inertial lift-up mechanism. This mechanism arises from stretching of polymer stress fluctuations by a base shear and, even in the absence of inertia, induces significant amplification that can trigger transition to elastic turbulence in rectilinear flows.
4. Input–output analysis quantifies the impact of forcing and energy content of velocity components. It reveals the influence of dimensionless groups (e.g., Reynolds and

Weissenberg numbers) on amplification of deterministic and stochastic disturbances and identifies relevant spatiotemporal scales as well as the dominant flow structures.

5. The input–output viewpoint provides a model-based approach to vibrational flow control, where zero-mean oscillations introduce a sensorless feedback to the original dynamics. Effective strategies for controlling the onset of turbulence and turbulence suppression have been designed by examining the dynamics of fluctuations around the base flow induced by spatiotemporal oscillations.
6. Linearized Navier–Stokes equations with stochastic forcing qualitatively predict structural features of turbulent shear flows and provide sufficient flexibility to account for two-point correlations of fully developed turbulence via low-complexity models.
7. The input–output framework provides a data-driven refinement of a physics-based model, guarantees statistical consistency, and captures complex dynamics of turbulent flows in a way that is tractable for analysis, optimization, and control design.
8. Tools and ideas from control theory and convex optimization overcome shortcomings of physics-agnostic machine learning algorithms and enable the development of theory and techniques for physics-aware data-driven turbulence modeling.

## FUTURE ISSUES

1. Complex fluids and complex flows: Among other emerging applications, input–output analysis is expected to clarify the importance of different physical mechanisms in the presence of surface roughness and free-stream disturbances and to quantify the impact of modeling uncertainties that arise from chemical reactions and gas surface interactions in hypersonic flows (Candler 2019).
2. Computational complexity: For an evolution model with  $n$  degrees of freedom, the tools presented in this review require  $\mathcal{O}(n^3)$  computations. Such computations are routine for canonical flows, but the large-scale nature of spatially discretized models in complex geometries induces significant computational overhead.
3. Nonlinear interactions: Precise characterization of the interplay between high flow sensitivity and nonlinearity in order to capture later stages of disturbance development, identify possible routes for transition, and design effective control strategies for the nonlinear Navier–Stokes equations remains a grand challenge.
4. Data-driven techniques: In spite of the apparent promise of machine and reinforcement learning, several challenges have to be addressed, including the development of methods that respect physical constraints, generalize to flow regimes that are not accounted for in the available data, and offer convergence, performance, and robustness guarantees on par with model-based approaches to flow control.
5. Feedback control: A host of challenges, including estimation using noisy measurements, optimal sensor and actuator placement, efficient computation of optimal and robust controllers, structured and distributed control synthesis, and convergence and sample complexity of data-driven reinforcement learning strategies, have to be addressed to enable a successful feedback control at high Reynolds numbers.

## DISCLOSURE STATEMENT

The author is not aware of any biases that might be perceived as affecting the objectivity of this review.

## ACKNOWLEDGMENTS

I would like to thank Bassam Bamieh for his mentorship, friendship, and support over the years. Bassam inspired me to work at the interface between fluid mechanics and control and has been an intellectual role model for me from the first day we met. I am grateful to Parviz Moin for welcoming me to the Center for Turbulence Research at Stanford University on numerous occasions; these visits pushed me out of my comfort zone and made me a better researcher. I am indebted to Makan Fardad, Tryphon Georgiou, Satish Kumar, Joe Nichols, and Peter Schmid for our collaborations and for their thoughtful feedback about this review; we enjoy spending time with each other and our scientific interactions are a consequence of our friendship. This work would not have been possible without contributions of my current and former PhD students Neil Dhingra, Anubhav Dwivedi, Gokul Hariharan, Nazish Hoda, Binh Lieu, Fu Lin, Rashad Moarref, Wei Ran, and Armin Zare and without support from the Air Force Office of Scientific Research under awards FA9550-16-1-0009 and FA9550-18-1-0422, and from the National Science Foundation under award ECCS-1809833.

## LITERATURE CITED

- Agarwal A, Brandt L, Zaki TA. 2014. Linear and nonlinear evolution of a localized disturbance in polymeric channel flow. *J. Fluid Mech.* 760:278–303
- Ahmadi M, Valmorbida G, Gayme D, Papachristodoulou A. 2019. A framework for input–output analysis of wall-bounded shear flows. *J. Fluid Mech.* 873:742–85
- Bamieh B, Dahleh M. 2001. Energy amplification in channel flows with stochastic excitation. *Phys. Fluids* 13:3258–69**
- Bandyopadhyay PR. 2006. Stokes mechanism of drag reduction. *J. Appl. Mech.* 73:483–89
- Beneddine S, Sipp D, Arnault A, Dandois J, Lesshafft L. 2016. Conditions for validity of mean flow stability analysis. *J. Fluid Mech.* 798:485–504
- Beneddine S, Yegavian R, Sipp D, Leclaire B. 2017. Unsteady flow dynamics reconstruction from mean flow and point sensors: an experimental study. *J. Fluid Mech.* 824:174–201
- Benner P, Li JR, Penzl T. 2008. Numerical solution of large-scale Lyapunov equations, Riccati equations, and linear-quadratic optimal control problems. *Numer. Linear Algebra Appl.* 15:755–77
- Bertolotti FP, Herbert T. 1991. Analysis of the linear stability of compressible boundary layers using the PSE. *Theor. Comput. Fluid Dyn.* 3:117–24
- Bewley TR. 2009. A fundamental limit on the balance of power in a transpiration-controlled channel flow. *J. Fluid Mech.* 632:443–46
- Bewley TR, Liu S. 1998. Optimal and robust control and estimation of linear paths to transition. *J. Fluid Mech.* 365:305–49
- Bewley TR, Luchini P, Pralits J. 2016. Methods for solution of large optimal control problems that bypass open-loop model reduction. *Meccanica* 51:2997–3014
- Bird RB, Curtiss CF, Armstrong RC, Hassager O. 1987. *Dynamics of Polymeric Liquids*, Vol. 2. New York: Wiley. 2nd ed.
- Boyd JP. 2001. *Chebyshev and Fourier Spectral Methods*. New York: Dover. 2nd ed.
- Boyd S, Vandenberghe L. 2004. *Convex Optimization*. Cambridge, UK: Cambridge Univ. Press
- Brandt L, Sipp D, Pralits JO, Marquet O. 2011. Effect of base-flow variation in noise amplifiers: the flat-plate boundary layer. *J. Fluid Mech.* 687:503–28

Provides a Reynolds  
number scaling of  
energy amplification.

- Brunton SL, Noack BR, Koumoutsakos P. 2020. Machine learning for fluid mechanics. *Annu. Rev. Fluid Mech.* 52:477–508
- Butler KM, Farrell BF. 1992. Three-dimensional optimal perturbations in viscous shear flow. *Phys. Fluids A* 4:1637
- Butler KM, Farrell BF. 1993. Optimal perturbations and streak spacing in wall-bounded turbulent shear flow. *Phys. Fluids A* 5:774–77
- Candler GV. 2019. Rate effects in hypersonic flows. *Annu. Rev. Fluid Mech.* 51:379–402
- Chavarin A, Luhar M. 2020. Resolvent analysis for turbulent channel flow with riblets. *ALAA J.* 58:589–99
- Chen KK, Rowley CW. 2011.  $H_2$  optimal actuator and sensor placement in the linearised complex Ginzburg–Landau system. *J. Fluid Mech.* 681:241–60
- Chevalier M, Hoepffner J, Bewley TR, Henningson DS. 2006. State estimation in wall-bounded flow systems. Part 2. Turbulent flows. *J. Fluid Mech.* 552:167–87
- Choi KS. 2002. Near-wall structure of turbulent boundary layer with spanwise-wall oscillation. *Phys. Fluids* 14:2530–42
- Choi KS, DeBisschop JR, Clayton BR. 1998. Turbulent boundary-layer control by means of spanwise-wall oscillation. *ALAA J.* 36:1157–63
- Cossu C, Pujals G, Depardon S. 2009. Optimal transient growth and very large-scale structures in turbulent boundary layers. *J. Fluid Mech.* 619:79–94
- del Álamo JC, Jiménez J. 2003. Spectra of the very large anisotropic scales in turbulent channels. *Phys. Fluids* 15:41–44
- del Álamo JC, Jiménez J. 2006. Linear energy amplification in turbulent channels. *J. Fluid Mech.* 559:205–13
- del Álamo JC, Jiménez J, Zandonade P, Moser RD. 2004. Scaling of the energy spectra of turbulent channels. *J. Fluid Mech.* 500:135–44
- Dhanak M, Si C. 1999. On reduction of turbulent wall friction through spanwise wall oscillations. *J. Fluid Mech.* 383:175–95
- Dhingra NK, Jovanović MR, Luo ZQ. 2014. An ADMM algorithm for optimal sensor and actuator selection. In *Proceedings of the 53rd IEEE Conference on Decision and Control*, pp. 4039–44. New York: IEEE
- Duraisamy K, Iaccarino G, Xiao H. 2019. Turbulence modeling in the age of data. *Annu. Rev. Fluid Mech.* 51:357–77
- Dwivedi A, Hildebrand N, Nichols JV, Candler GV, Jovanović MR. 2020. Transient growth analysis of oblique shock wave/boundary-layer interactions at Mach 5.92. *Phys. Rev. Fluids* 5:063904
- Dwivedi A, Sidharth GS, Nichols JW, Candler GV, Jovanović MR. 2019. Reattachment vortices in hypersonic compression ramp flow: an input–output analysis. *J. Fluid Mech.* 880:113–35
- Farrell BF, Ioannou PJ. 1993. Stochastic forcing of the linearized Navier–Stokes equations. *Phys. Fluids A* 5:2600–9
- Farrell BF, Ioannou PJ. 2012. Dynamics of streamwise rolls and streaks in turbulent wall-bounded shear flow. *J. Fluid Mech.* 708:149–96
- Fazel M. 2002. *Matrix rank minimization with applications*. PhD Thesis, Stanford Univ., Stanford, CA
- Fedorov A. 2011. Transition and stability of high-speed boundary layers. *Annu. Rev. Fluid Mech.* 43:79–95
- Fransson JHM, Talamelli A, Brandt L, Cossu C. 2006. Delaying transition to turbulence by a passive mechanism. *Phys. Rev. Lett.* 96:064501
- Fukagata K, Sugiyama K, Kasagi N. 2009. On the lower bound of net driving power in controlled duct flows. *Physica D* 238:1082–86
- Gardner W. 1990. *Introduction to Random Processes: With Applications to Signals and Systems*. New York: McGraw-Hill
- Garnaud X, Sandberg RD, Lesshafft L. 2013. *Global response to forcing in a subsonic jet: instability wavepackets and acoustic radiation*. Paper presented at AIAA/CEAS Aeroacoustics Conference, 19th, Berlin, AIAA Pap. 2013-2232
- Georgiou TT. 2002a. Spectral analysis based on the state covariance: the maximum entropy spectrum and linear fractional parametrization. *IEEE Trans. Autom. Control* 47:1811–23
- Georgiou TT. 2002b. The structure of state covariances and its relation to the power spectrum of the input. *IEEE Trans. Autom. Control* 47:1056–66

---

Provides a transient growth analysis of transition.

---



---

Provides a transient growth analysis of eddy viscosity-enhanced linearized NS equations.

---



---

Provides an input–output analysis of hypersonic flow.

---



---

Provides a first use of the linearized NS equations with stochastic forcing to study transition.

---

Provides, along with Hoda et al. (2009), an input–output analysis of viscoelastic fluids.

Provides, along with Hwang & Cossu (2010b), an input–output analysis of eddy–viscosity enhanced linearized NS equations.

Provides an input–output analysis of jet noise.

Provides a componentwise input–output analysis of transition: a more informative tool than resolvent analysis.

Discovers, along with Jovanović & Kumar (2011), a viscoelastic lift-up mechanism.

- Groisman A, Steinberg V. 2000. Elastic turbulence in a polymer solution flow. *Nature* 405:53–55
- Gustavsson LH. 1991. Energy growth of three-dimensional disturbances in plane Poiseuille flow. *J. Fluid Mech.* 224:241–60
- Halko N, Martinsson PG, Tropp JA. 2011. Finding structure with randomness: probabilistic algorithms for constructing approximate matrix decompositions. *SIAM Rev.* 53:217–88
- Hariharan G, Jovanović MR, Kumar S. 2018. Amplification of localized body forces in channel flows of viscoelastic fluids. *J. Non-Newton. Fluid Mech.* 260:40–53
- Hildebrand N, Dwivedi A, Nichols JW, Jovanović MR, Candler GV. 2018. Simulation and stability analysis of oblique shock wave/boundary layer interactions at Mach 5.92. *Phys. Rev. Fluids* 3:013906
- Hoda N, Jovanović MR, Kumar S. 2008. Energy amplification in channel flows of viscoelastic fluids. *J. Fluid Mech.* 601:407–24**
- Hoda N, Jovanović MR, Kumar S. 2009. Frequency responses of streamwise-constant perturbations in channel flows of Oldroyd-B fluids. *J. Fluid Mech.* 625:411–34
- Hoepffner J. 2005. Modeling flow statistics using convex optimization. In *Proceedings of the 2005 European Control Conference and the 44th IEEE Conference on Decision and Control*, pp. 4287–92. New York: IEEE
- Hoepffner J, Chevalier M, Bewley TR, Henningson DS. 2005. State estimation in wall-bounded flow systems. Part 1. Perturbed laminar flows. *J. Fluid Mech.* 534:263–94
- Hoepffner J, Fukagata K. 2009. Pumping or drag reduction? *J. Fluid Mech.* 635:171–87
- Högberg M, Bewley TR, Henningson DS. 2003a. Linear feedback control and estimation of transition in plane channel flow. *J. Fluid Mech.* 481:149–75
- Högberg M, Bewley TR, Henningson DS. 2003b. Relaminarization of  $Re_\tau = 100$  turbulence using linear state-feedback control. *Phys. Fluids* 15:3572–75
- Hwang Y, Cossu C. 2010a. Amplification of coherent streaks in the turbulent Couette flow: an input–output analysis at low Reynolds number. *J. Fluid Mech.* 643:333–48**
- Hwang Y, Cossu C. 2010b. Linear non-normal energy amplification of harmonic and stochastic forcing in the turbulent channel flow. *J. Fluid Mech.* 664:51–73
- Hwang Y, Eckhardt B. 2020. Attached eddy model revisited using a minimal quasi-linear approximation. *J. Fluid Mech.* 894:A23
- Jeun J, Nichols JW, Jovanović MR. 2016. Input-output analysis of high-speed axisymmetric isothermal jet noise. *Phys. Fluids* 28:047101**
- Jordan P, Colonius T. 2013. Wave packets and turbulent jet noise. *Annu. Rev. Fluid Mech.* 45:173–95
- Joshi SS, Speyer JL, Kim J. 1997. A systems theory approach to the feedback stabilization of infinitesimal and finite-amplitude disturbances in plane Poiseuille flow. *J. Fluid Mech.* 332:157–84
- Jovanović MR. 2004. *Modeling, analysis, and control of spatially distributed systems*. PhD Thesis, Univ. California, Santa Barbara
- Jovanović MR. 2008. Turbulence suppression in channel flows by small amplitude transverse wall oscillations. *Phys. Fluids* 20:014101
- Jovanović MR, Bamieh B. 2001. Modelling flow statistics using the linearized Navier-Stokes equations. In *Proceedings of the 40th IEEE Conference on Decision and Control*, pp. 4944–49. New York: IEEE
- Jovanović MR, Bamieh B. 2005. Componentwise energy amplification in channel flows. *J. Fluid Mech.* 534:145–83**
- Jovanović MR, Fardad M. 2008.  $H_2$  norm of linear time-periodic systems: a perturbation analysis. *Automatica* 44:2090–98
- Jovanović MR, Georgiou TT. 2010. *Reproducing second order statistics of turbulent flows using linearized Navier-Stokes equations with forcing*. Paper presented at 63rd Annual Meeting of the APS Division of Fluid Dynamics, Long Beach, CA, Nov. 21
- Jovanović MR, Kumar S. 2010. Transient growth without inertia. *Phys. Fluids* 22:023101**
- Jovanović MR, Kumar S. 2011. Nonmodal amplification of stochastic disturbances in strongly elastic channel flows. *J. Non-Newton. Fluid Mech.* 166:755–78
- Jovanović MR, Schmid PJ, Nichols JW. 2014. Sparsity-promoting dynamic mode decomposition. *Phys. Fluids* 26:024103
- Jung W, Mangiavacchi N, Akhavan R. 1992. Suppression of turbulence in wall-bounded flows by high-frequency spanwise oscillations. *Phys. Fluids A* 4:1605–7



- Kalur A, Seiler PJ, Hemati M. 2020. *Stability and performance analysis of nonlinear and non-normal systems using quadratic constraints*. Paper presented at the 2020 AIAA SciTech Forum and Exposition, Orlando, FL, AIAA Pap. 2020-0833
- Kerswell RR. 2018. Nonlinear nonmodal stability theory. *Annu. Rev. Fluid Mech.* 50:319–45
- Kim J, Bewley TR. 2007. A linear systems approach to flow control. *Annu. Rev. Fluid Mech.* 39:383–417
- Kim J, Lim J. 2000. A linear process in wall-bounded turbulent shear flows. *Phys. Fluids* 12:1885–88
- Kim J, Moin P, Moser R. 1987. Turbulence statistics in fully developed channel flow at low Reynolds number. *J. Fluid Mech.* 177:133–66
- Kwakernaak H, Sivan R. 1972. *Linear Optimal Control Systems*. New York: Wiley
- Laadhari F, Skandaji L, Morel R. 1994. Turbulence reduction in a boundary layer by a local spanwise oscillating surface. *Phys. Fluids* 6:3218–20
- Landahl MT. 1975. Wave breakdown and turbulence. *SIAM J. Appl. Math.* 28:735–56**
- Larson RG, Shaqfeh ESG, Muller SJ. 1990. A purely elastic instability in Taylor–Couette flow. *J. Fluid Mech.* 218:573–600
- Lee C, Min T, Kim J. 2008. Stability of a channel flow subject to wall blowing and suction in the form of a traveling wave. *Phys. Fluids* 20:101513
- Lee MJ, Kim J, Moin P. 1990. Structure of turbulence at high shear rate. *J. Fluid Mech.* 216:561–83
- Lieu BK, Jovanović MR, Kumar S. 2013. Worst-case amplification of disturbances in inertialess Couette flow of viscoelastic fluids. *J. Fluid Mech.* 723:232–63
- Lieu BK, Moarref R, Jovanović MR. 2010. Controlling the onset of turbulence by streamwise traveling waves. Part 2: direct numerical simulations. *J. Fluid Mech.* 663:100–19
- Lin F, Fardad M, Jovanović MR. 2013. Design of optimal sparse feedback gains via the alternating direction method of multipliers. *IEEE Trans. Autom. Control* 58:2426–31
- Lin F, Jovanović MR. 2009. Least-squares approximation of structured covariances. *IEEE Trans. Autom. Control* 54:1643–48
- Luhar M, Sharma AS, McKeon BJ. 2014. Opposition control within the resolvent analysis framework. *J. Fluid Mech.* 749:597–626
- Lumley JL. 2007. *Stochastic Tools in Turbulence*. Mineola, NY: Dover
- Malik MR. 1989. Prediction and control of transition in supersonic and hypersonic boundary layers. *AIAA J.* 27:1487–93
- Malkus WVR. 1956. Outline of a theory of turbulent shear flow. *J. Fluid Mech.* 1:521–39
- Marusic I, Joseph DD, Mahesh K. 2007. Laminar and turbulent comparisons for channel flow and flow control. *J. Fluid Mech.* 570:467–77
- McKeon BJ, Sharma AS. 2010. A critical-layer framework for turbulent pipe flow. *J. Fluid Mech.* 658:336–82**
- McMullen RM, Rosenberg K, McKeon BJ. 2020. Interaction of forced Orr–Sommerfeld and Squire modes in a low-order representation of turbulent channel flow. arXiv:2001.02785 [physics.flu-dyn]
- Megretski A, Rantzer A. 1997. System analysis via integral quadratic constraints. *IEEE Trans. Autom. Control* 42:819–30
- Min T, Kang SM, Speyer JL, Kim J. 2006. Sustained sub-laminar drag in a fully developed channel flow. *J. Fluid Mech.* 558:309–18**
- Moarref R, Jovanović MR. 2010. Controlling the onset of turbulence by streamwise traveling waves. Part 1: receptivity analysis. *J. Fluid Mech.* 663:70–99**
- Moarref R, Jovanović MR. 2012. Model-based design of transverse wall oscillations for turbulent drag reduction. *J. Fluid Mech.* 707:205–40**
- Moarref R, Jovanović MR, Tropp JA, Sharma AS, McKeon BJ. 2014. A low-order decomposition of turbulent channel flow via resolvent analysis and convex optimization. *Phys. Fluids* 26:051701
- Moarref R, Sharma AS, Tropp JA, McKeon BJ. 2013. Model-based scaling of the streamwise energy density in high-Reynolds-number turbulent channels. *J. Fluid Mech.* 734:275–316
- Mohammadi H, Zare A, Soltanolkotabi M, Jovanović MR. 2019. Convergence and sample complexity of gradient methods for the model-free linear quadratic regulator problem. arXiv:1912.11899 [math.OC]
- Moin P, Moser RD. 1989. Characteristic-eddy decomposition of turbulence in a channel. *J. Fluid Mech.* 200:471–509

---

**Discovers a lift-up mechanism.**

---



---

**Provides a resolvent analysis of turbulent flow.**

---



---

**Demonstrates a sublaminar drag via traveling waves.**

---



---

**Provides a model-based design of traveling waves.**

---



---

**Provides a model-based design of wall oscillations.**

---

---

Provides an input-output analysis of boundary layer with stochastic forcing.

---

Provides, along with Chavarin & Luhar (2020), an input-output analysis of turbulent channel flow with riblets.

---



---

Provides an outstanding review of nonmodal stability theory.

---



---

Provides an input-output analysis of boundary layer.

---

- Morra P, Semeraro O, Henningson DS, Cossu C. 2019. On the relevance of Reynolds stresses in resolvent analyses of turbulent wall-bounded flows. *J. Fluid Mech.* 867:969–84
- Noack BR, Morzyński M, Tadmor G. 2011. *Reduced-Order Modelling for Flow Control*. Vienna: Springer-Verlag
- Odeh F, Keller JB. 1964. Partial differential equations with periodic coefficients and Bloch waves in crystals. *J. Math. Phys.* 5:1499–504
- Page J, Zaki TA. 2014. Streak evolution in viscoelastic Couette flow. *J. Fluid Mech.* 742:520–51
- Pope SB. 2000. *Turbulent Flows*. Cambridge, UK: Cambridge Univ. Press
- Pujals G, García-Villalba M, Cossu C, Depardon S. 2009. A note on optimal transient growth in turbulent channel flows. *Phys. Fluids* 21:015109
- Qin B, Salipante PF, Hudson SD, Arratia PE. 2019a. Flow resistance and structures in viscoelastic channel flows at low  $Re$ . *Phys. Rev. Lett.* 123:194501
- Qin B, Salipante PF, Hudson SD, Arratia PE. 2019b. Upstream vortex and elastic wave in the viscoelastic flow around a confined cylinder. *J. Fluid Mech.* 864:R2
- Quadrio M, Ricco P. 2004. Critical assessment of turbulent drag reduction through spanwise wall oscillations. *J. Fluid Mech.* 521:251–71
- Ran W, Zare A, Hack MJP, Jovanović MR. 2019a. Modeling mode interactions in boundary layer flows via parabolized Floquet equations. *Phys. Rev. Fluids* 4:023901
- Ran W, Zare A, Hack MJP, Jovanović MR. 2019b. Stochastic receptivity analysis of boundary layer flow. *Phys. Rev. Fluids* 4:093901**
- Ran W, Zare A, Jovanović MR. 2020. Model-based design of riblets for turbulent drag reduction. *J. Fluid Mech.* In press**
- Recht B, Fazel M, Parrilo PA. 2010. Guaranteed minimum-rank solutions of linear matrix equations via nuclear norm minimization. *SIAM Rev.* 52:471–501
- Reynolds WC, Hussain AKMF. 1972. The mechanics of an organized wave in turbulent shear flow. Part 3. Theoretical models and comparisons with experiments. *J. Fluid Mech.* 54:263–88
- Reynolds WC, Tiederman WG. 1967. Stability of turbulent channel flow with application to Malkus's theory. *J. Fluid Mech.* 27:253–72
- Ricco P. 2004. Modification of near-wall turbulence due to spanwise wall oscillations. *J. Turbul.* 5:N24
- Ricco P. 2011. Laminar streaks with spanwise wall forcing. *Phys. Fluids* 23:064103
- Ricco P, Quadrio M. 2008. Wall-oscillation conditions for drag reduction in turbulent channel flow. *Int. J. Heat Fluid Flow* 29:891–902
- Rigas G, Sipp D, Colonius T. 2020. Non-linear input/output analysis: application to boundary layer transition. arXiv:2001.09440 [physics.flu-dyn]
- Rosenberg K, McKeon BJ. 2019. Efficient representation of exact coherent states of the Navier–Stokes equations using resolvent analysis. *Fluid Dyn. Res.* 51:011401
- Rowley CW. 2005. Model reduction for fluids using balanced proper orthogonal decomposition. *Int. J. Bifurc. Chaos* 15:997–1013
- Rowley CW, Dawson ST. 2017. Model reduction for flow analysis and control. *Annu. Rev. Fluid Mech.* 49:387–417
- Schmid PJ. 2007. Nonmodal stability theory. *Annu. Rev. Fluid Mech.* 39:129–62**
- Schmid PJ. 2010. Dynamic mode decomposition of numerical and experimental data. *J. Fluid Mech.* 656:5–28
- Schmid PJ, Henningson DS. 2001. *Stability and Transition in Shear Flows*. New York: Springer
- Sidharth G, Dwivedi A, Candler GV, Nichols JW. 2018. Onset of three-dimensionality in supersonic flow over a slender double wedge. *Phys. Rev. Fluids* 3:093901
- Sipp D, Marquet O. 2013. Characterization of noise amplifiers with global singular modes: the case of the leading-edge flat-plate boundary layer. *Theor. Comput. Fluid Dyn.* 27:617–35**
- Tadmor G, Noack BR. 2011. Bernoulli, Bode, and budgie. *IEEE Control Syst. Mag.* 31(2):18–23
- Thomas VL, Lieu BK, Jovanović MR, Farrell BF, Ioannou PJ, Gayme DF. 2014. Self-sustaining turbulence in a restricted nonlinear model of plane Couette flow. *Phys. Fluids* 26:105112
- Toedtli SS, Luhar M, McKeon BJ. 2019. Predicting the response of turbulent channel flow to varying-phase opposition control: resolvent analysis as a tool for flow control design. *Phys. Rev. Fluids* 4:073905
- Towne A, Lozano-Durán A, Yang X. 2020. Resolvent-based estimation of space-time flow statistics. *J. Fluid Mech.* 883:A17

- Towne A, Schmidt OT, Colonius T. 2018. Spectral proper orthogonal decomposition and its relationship to dynamic mode decomposition and resolvent analysis. *J. Fluid Mech.* 847:821–67
- Trefethen LN, Embree M. 2005. *Spectra and Pseudospectra: The Behavior of Nonnormal Matrices and Operators*. Princeton, NJ: Princeton Univ. Press
- Trefethen LN, Trefethen AE, Reddy SC, Driscoll TA. 1993. Hydrodynamic stability without eigenvalues. *Science* 261:578–84
- Waleffe F. 1997. On a self-sustaining process in shear flows. *Phys. Fluids* 9:883–900
- Weideman JAC, Reddy SC. 2000. A MATLAB differentiation matrix suite. *ACM Trans. Math. Softw.* 26:465–519
- Zare A, Chen Y, Jovanović MR, Georgiou TT. 2017a. Low-complexity modeling of partially available second-order statistics: theory and an efficient matrix completion algorithm. *IEEE Trans. Autom. Control* 62:1368–83
- Zare A, Georgiou TT, Jovanović MR. 2020a. Stochastic dynamical modeling of turbulent flows. *Annu. Rev. Control Robot. Auton. Syst.* 3:195–219
- Zare A, Jovanović MR, Georgiou TT. 2017b. Colour of turbulence. *J. Fluid Mech.* 812:636–80
- Zare A, Mohammadi H, Dhingra NK, Georgiou TT, Jovanović MR. 2020b. Proximal algorithms for large-scale statistical modeling and sensor/actuator selection. *IEEE Trans. Autom. Control* 65:3441–56
- Zhou K, Doyle JC, Glover K. 1996. *Robust and Optimal Control*. Upper Saddle River, NJ: Prentice-Hall

---

Must-read; provides the first use of resolvent analysis and pseudo-spectra in fluid mechanics.

---

Discovers a self-sustaining mechanism.

---

Provides turbulence modeling using the linearized NS equations with stochastic forcing.

---

Develops, along with Dhingra et al. (2014), algorithms for optimal sensor and actuator placement.

---



# Contents

Leonardo da Vinci and Fluid Mechanics <i>Ivan Marusic and Susan Broomhall</i> .....	1
Elastic Turbulence: An Experimental View on Inertialess Random Flow <i>Victor Steinberg</i> .....	27
Turbulence Processes Within Turbidity Currents <i>Mathew G. Wells and Robert M. Dorrell</i> .....	59
Statistics of Extreme Events in Fluid Flows and Waves <i>Themistoklis P. Sapsis</i> .....	85
Layering, Instabilities, and Mixing in Turbulent Stratified Flows <i>C.P. Caulfield</i> .....	113
The Fluid Mechanics of Cleaning and Decontamination of Surfaces <i>Julien R. Landel and D. Ian Wilson</i> .....	147
Mixing by Oceanic Lee Waves <i>Sonya Legg</i> .....	173
Levitation and Self-Organization of Droplets <i>Vladimir S. Ajaev and Oleg A. Kabov</i> .....	203
Exact Coherent States and the Nonlinear Dynamics of Wall-Bounded Turbulent Flows <i>Michael D. Graham and Daniel Floryan</i> .....	227
Statistical Properties of Subgrid-Scale Turbulence Models <i>Robert D. Moser, Sigfried W. Haering, and Gopal R. Yalla</i> .....	255
The Fluid Mechanics of Tidal Stream Energy Conversion <i>Thomas A.A. Adcock, Scott Draper, Richard H.J. Willden, and Christopher R. Vogel</i> ...	287
From Bypass Transition to Flow Control and Data-Driven Turbulence Modeling: An Input–Output Viewpoint <i>Mihailo R. Jovanović</i> .....	311
Bluff Bodies and Wake–Wall Interactions <i>Mark C. Thompson, Thomas Leweke, and Kerry Hourigan</i> .....	347
Fluids at the Nanoscale: From Continuum to Subcontinuum Transport <i>Nikita Kavokine, Roland R. Netz, and Lydéric Bocquet</i> .....	377

In Pursuit of Designing Multicellular Engineered Living Systems: A Fluid Mechanical Perspective <i>Jean Carlos Serrano, Satish Kumar Gupta, Roger D. Kamm, and Ming Guo</i> .....	411
Predicting the Drag of Rough Surfaces <i>Daniel Chung, Nicholas Hutchins, Michael P. Schultz, and Karen A. Flack</i> .....	439
The Fluid Dynamics of Disease Transmission <i>Lydia Bourouiba</i> .....	473
Numerical Methods for Viscoelastic Fluid Flows <i>M.A. Alves, P.J. Oliveira, and F.T. Pinho</i> .....	509
X-Ray Flow Visualization in Multiphase Flows <i>Alberto Aliseda and Theodore J. Heindel</i> .....	543

## Indexes

Cumulative Index of Contributing Authors, Volumes 1–53 .....	569
Cumulative Index of Article Titles, Volumes 1–53 .....	580

## Errata

An online log of corrections to *Annual Review of Fluid Mechanics* articles may be found at <http://www.annualreviews.org/errata/fluid>